

Broad-band ocean bottom seismometer noise properties

Helen A. Janiszewski¹, Z. Eilon,² J.B. Russell³, B. Brunsvik,² J.B. Gaherty,⁴ S.G. Mosher,⁵ W.B. Hawley⁶ and S. Coats¹

¹Department of Earth Sciences, University of Hawai‘i at Mānoa, Honolulu, HI 96822, USA. E-mail: hajanisz@hawaii.edu

²Department of Earth Science, University of California, Santa Barbara, CA 93106, USA

³Department of Earth, Environmental and Planetary Sciences, Brown University, Providence, RI 02912, USA

⁴School of Earth & Sustainability, Northern Arizona University, Flagstaff, AZ 86011, USA

⁵Department of Earth and Environmental Sciences, University of Ottawa, Ottawa, ON K1N 6N5, Canada

⁶Lamont-Doherty Earth Observatory of Columbia University, Palisades, NY 10964-1000, USA

Accepted 2022 November 16. Received 2022 November 11; in original form 2022 May 10

SUMMARY

We present a new compilation and analysis of broad-band ocean bottom seismometer noise properties from 15 yr of seismic deployments. We compile a comprehensive data set of representative four-component (seismometer and pressure gauge) noise spectra and cross-spectral properties (coherence, phase and admittance) for 551 unique stations spanning 18 U.S.-led experiments. This is matched with a comprehensive compilation of metadata parameters related to instrumentation and environmental properties for each station. We systematically investigate the similarity of noise spectra by grouping them according to these metadata parameters to determine which factors are the most important in determining noise characteristics. We find evidence for improvements in similarity of noise properties when grouped across parameters, with groupings by seismometer type and deployment water depth yielding the most significant and interpretable results. Instrument design, that is the entire deployed package, also plays an important role, although it strongly covaries with seismometer and water depth. We assess the presence of traditional sources of tilt, compliance, and microseismic noise to characterize their relative role across a variety of commonly used seismic frequency bands. We find that the presence of tilt noise is primarily dependent on the type of seismometer used (covariant with a particular subset of instrument design), that compliance noise follows anticipated relationships with water depth, and that shallow, oceanic shelf environments have systematically different microseism noise properties (which are, in turn, different from instruments deployed in shallow lake environments). These observations have important implications for the viability of commonly used seismic analysis techniques. Finally, we compare spectra and coherences before and after vertical channel tilt and compliance noise removal to evaluate the efficacy and limitations of these now standard processing techniques. These findings may assist in future experiment planning and instrument development, and our newly compiled noise data set serves as a building block for more targeted future investigations by the marine seismology community.

Key words: Seismic noise; Seismic instruments; Instrumental noise; Site effects; Pacific Ocean; Atlantic Ocean.

1 INTRODUCTION

Over recent decades, the marine seismological community has made steady progress in the deployment of increasingly high-quality and large(r)-N broad-band ocean-bottom seismometer (BBOBS) networks. It is approximately 30 yr since the advent of modern-standard ocean-floor seismic instruments (Cox *et al.* 1984; Montagner *et al.* 1994; Webb *et al.* 1994; Purdy & Orcutt 1995; Collins *et al.* 2001;

Stephen *et al.* 2003) led to the formation of the Ocean Bottom Seismic Instrument Pool (OBSIP) in 1999 (Aderhold *et al.* 2019). It is approximately 10 yr since the conception and execution of one of the most ambitious community BBOBS deployments to date: the Cascadia Initiative (Toomey *et al.* 2014). Systematic archiving of seismic and pressure-gauge data at the Incorporated Research Institutions for Seismology (IRIS) Data Management Center (DMC), along with community tools for preprocessing BBOBS data (e.g.

ATaCR, Janiszewski *et al.* 2019; DLOPy, Doran & Laske 2017) have substantially expanded the reach and salience of BBOBS data across the wider seismological community. With the recent reorganization of the national U.S. instrument pool into the Ocean Bottom Seismic Instrument Center (OBSIC), the emergence and expansion of improving hardware (Goncharov *et al.* 2016; Shinohara *et al.* 2018), renewed planning towards long-term BBOBS observatories (Kohler *et al.* 2020), and the evolution of new seafloor technologies (Spica *et al.* 2020; Lior *et al.* 2021), this is an apposite juncture to assess the systematics of BBOBS noise traits.

Analyses of spectra (including both seismometer and pressure-gauge data) for individual deployments suggest significant seismic noise variations exist among deployed BBOBSs (Yang *et al.* 2012; Sumy *et al.* 2015; Barchek *et al.* 2020; An *et al.* 2021). Direct comparisons of their noise have largely focused on single-instrument tests rather than arrays (Webb 1998), extrapolating vault sensor performance to *in situ* conditions (Stähler *et al.* 2018), or pilot studies that contrast different installation techniques (e.g. Collins *et al.* 2001). These are limited in location and do not include all types of BBOBS design in the modern OBSIC fleet. To date, a systematic noise comparison across deployments that encompasses the full range of instrument designs, water depths and site conditions does not exist. Recent analyses using the Cascadia Initiative data set demonstrate variability as a function of instrument design and water depth (Bell *et al.* 2015; Hilmo & Wilcock 2020), motivating expansion of such analyses across deployments.

In this study, we present a comprehensive data set describing the last 15 yr of U.S.-funded BBOBS array deployments (Fig. 1). We compute representative multicomponent noise spectra from stations deployed in a variety of environments, water depths, and using several different instrument designs. We calculate cross-channel coherences, upper and lower bounds on typical noise, and investigate systematics of noise within a variety of frequency bands spanning from 0.001 to 1 Hz. Using this data set, we offer a comprehensive and quantitative review of the character and sources of noise on BBOBS instruments.

2 BACKGROUND

2.1 Noise sources

The noise power spectrum from 0.001 to 1 Hz on BBOBS instruments is influenced by the presence and strength of microseism noise, infragravity waves, and tilt or bottom current noise. Microseism noise is characterized by a broad, high-amplitude peak between 0.05 and 0.5 Hz, and dominates the ambient seismic energy field world-wide (Peterson 1993; McNamara & Buland 2004). Its prevalence has resulted in the traditional distinction between ‘high frequency’ (>1 Hz) and ‘low frequency’ (<0.05 Hz) low-noise observational seismic bands. To first order, seafloor observations of microseismic noise globally are consistent with the long history of observations on land. The noise spectrum in this band is typically divided into two peaks—the secondary microseism, with multiple subpeaks at frequencies within 0.1–0.5 Hz (Stephen *et al.* 2003) and a dominant global peak located at ~ 0.14 Hz, and the primary microseism, which peaks at ~ 0.07 Hz (Webb 1998; Fig. 2).

Acoustic waves produced by the interaction of wind-generated ocean waves with the seafloor constitute the secondary microseism (Longuet-Higgins 1950). Several dominant mechanisms generate these interacting waves, including storm-generated swell, coastline reflected waves, and interactions of waves generated by multiple

storms (Bromirski *et al.* 2005; Ardhuin *et al.* 2011). Broadly, the amplitudes of higher frequency energy within the secondary microseism correlate with the local sea state, while waves generated from distant storms and their coastal reflections play a more important role at longer periods within this band (Babcock *et al.* 1994; Stephen *et al.* 2003; Bromirski *et al.* 2005). These properties can lead to systematic differences between ocean basins. The Pacific Ocean appears to propagate energy from larger, more distant storms with higher sustained wind speeds, leading to a secondary microseism peak that extends to lower frequencies than in the North Atlantic Ocean (Babcock *et al.* 1994; Webb 1998), although only limited numbers of instruments were used for these early measurements. More recently, Yang *et al.* (2012) observed systematic differences in long period microseismic energy between BBOBSs deployed in the South Pacific and the Tasman Sea off opposite coasts of New Zealand, with instruments in the marginal sea relatively deficient in longer period energy. Additionally, the secondary microseism peak may shift to higher frequencies in lake environments (Xu *et al.* 2017; Smalls *et al.* 2019).

The primary microseism peak is generated by direct interaction (shoaling) of ocean waves with the shoreline and rough seafloor topography (Hasselmann 1963; Ardhuin 2018). In the deep ocean, the primary microseism peak is weaker than the secondary microseism (Ardhuin *et al.* 2015). At longer periods than the primary microseism is a noise spectral-amplitude minimum termed the ‘noise notch’ (Webb 1998; Fig. 2a). Significant differences exist in the microseism properties between deep and shallow water; in shallow water, the primary microseism has higher amplitudes than the secondary microseism due to the direct coupling between the ocean swell with the seafloor (Webb & Crawford 2010; Hilmo & Wilcock 2020). This also reduces or removes the noise notch at shallow BBOBS (Hilmo & Wilcock 2020; Fig. 2b).

At lower frequencies still, noise from infragravity waves and bottom-currents is prevalent in BBOBS data. These signals are largely absent or strongly diminished at onshore sites. Infragravity waves are long period ($<\sim 0.03$ Hz) ocean waves generated in coastal regions. Typically, these have maximum amplitudes along the continental shelves, but a small amount of infragravity wave energy may reach and subsequently propagate efficiently across the open ocean (Webb *et al.* 1991; Uchiyama & McWilliams 2008; Ardhuin *et al.* 2014). Propagation into the deep ocean depends on coastal morphology (Aucan & Ardhuin 2013; Crawford *et al.* 2015; Bogiatzis *et al.* 2020). Infragravity waves in the deep ocean perturb the seafloor at long (>40 km) wavelength, such that coherent signals are observed on the seismic and pressure channels of BBOBSs (Crawford *et al.* 1991). On the seismometers, this compliance noise is strongest on the vertical component. Compliance noise also affects horizontal components, but is typically obscured by other noise sources, chiefly the effects of seafloor currents (Webb *et al.* 1991; Doran & Laske 2016). The pressure perturbations associated with infragravity waves have a frequency-dependent decay with depth in the water column. As a result, the maximum frequency at which seafloor compliance affects BBOBSs decreases in deeper water (Crawford & Webb 2000; Bell *et al.* 2015), and the minimum frequency extends beyond the low-frequency end of the sensitivity of modern instruments (Fig. 2).

Bottom-current noise is a consequence of seafloor currents directly buffeting the instrument (Webb 1998; Collins *et al.* 2001), and is impacted by the overall design profile of the BBOBS, including interactions with ropes and antennae attached to the instrument (Stähler *et al.* 2018; Essing *et al.* 2021). It affects the entire seismic band (Webb 1998), but is strongest at frequencies <0.1 Hz, and

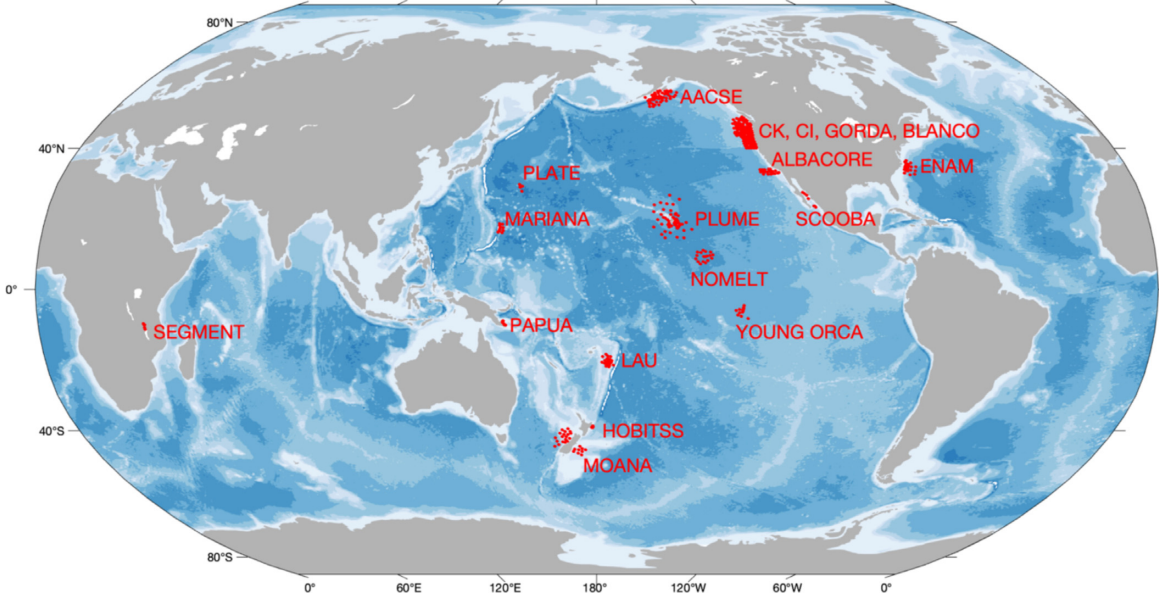


Figure 1. Map of analysed BBOBSs (red circles). Details corresponding to each deployment are given in Table S1. Made using M_Map (Pawlowicz 2020).

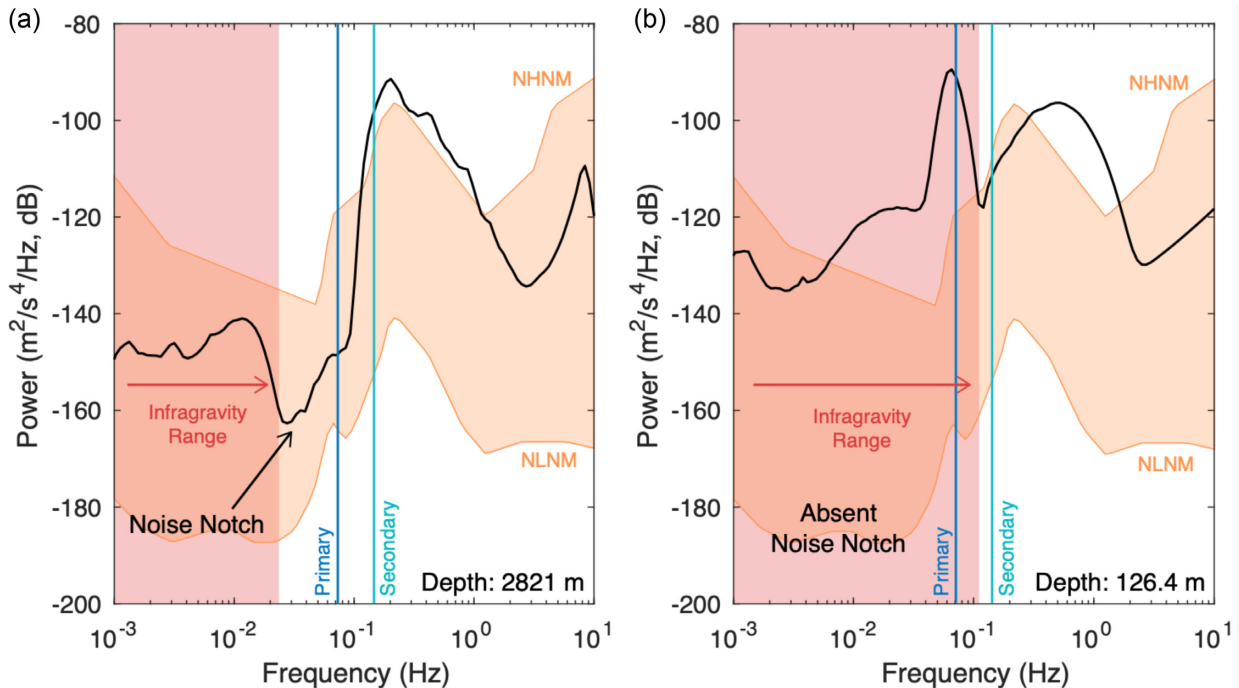


Figure 2. Examples of noise spectra for the Z component of a BBOBS for (a) deep-water station J36A and (b) shallow-water station M08A, both from the Cascadia Initiative. The noise notch and infragravity bands are labelled with frequencies adjusted for each individual station. The global primary (0.07 Hz) and secondary (0.14 Hz) microseism frequency peaks are labelled for illustrative purposes. The Peterson (1993) nominal high and low noise models are shown in orange.

leads to substantially higher noise levels on the horizontal components. In the case that the sensor is not perfectly level, this bottom-current noise can also couple into the vertical component, resulting in tilt noise (Crawford & Webb 2000). These follow a power-law increase with decreasing frequency. Current noise is analogous to wind-driven noise in land stations, but generally much stronger. On horizontal components, this noise largely eliminates the traditional low-noise observational band at frequencies below the microseism; analyses of earthquake signals on these components are generally

limited to high-amplitude recordings (i.e. large magnitude and/or nearby events).

2.2 Noise corrections

Tilt and compliance noise imply predictable relationships between the vertical and horizontal, and vertical and pressure time-series, respectively, at an individual BBOBS. Transfer functions quantify the admittance, coherence and phase relationships (in frequency

space) between these components (see Crawford & Webb 2000; Bell *et al.* 2015). Vertical seismic components can be corrected for tilt and compliance noise using the appropriate transfer functions (Crawford & Webb 2000), leading to a reduction of noise levels on this component. The approach relies on the statistical property of signal stationarity: temporally consistent transfer functions can be obtained by averaging frequency-domain relationships between components across multiple time windows. Typical approaches for calculating transfer functions include averaging over long time periods, such that transient signals occupy a relatively small percentage of time windows (Yang *et al.* 2012), or removing transient signals prior to processing (Bell *et al.* 2015; Janiszewski *et al.* 2019).

Seafloor compliance is theoretically a time-invariant property describing the response of the local subsurface to infragravity waves, and its admittance spectrum can be inverted for shallow shear velocity structure (e.g. Crawford *et al.* 1991; Ruan *et al.* 2014; Doran & Laske 2019; Mosher *et al.* 2021). This implies that an effective compliance correction can be obtained from a small number of time-averaged transfer functions. However, tilt can vary with time, as instruments settle in soft sediment and the degree and azimuth of non-verticality change. Some instruments also perform gyroscopic releveling cycles, with varying periodicity (Bell *et al.* 2015). To address these issues, tilt corrections derived from shorter-duration (e.g. daily) transfer functions may prove more effective (e.g. Bell *et al.* 2015).

3 METHODS

3.1 Inclusion criteria

Our study includes BBOBSs deployed as part of experiments facilitated by OBSIP or OBSIC from 2005 to the present. Each BBOBS in our data set satisfies the following criteria. (1) It contains a 3-component, wideband or broad-band seismometer (i.e. with flat instrument response between ~ 0.01 and ~ 10 Hz). We restrict our analysis to BBOBS designs with seismometers that are still actively used in the OBSIC fleet, which includes Guralp CMG-3T (CMG-3T), Nanometrics Trillium Compact (T-Compact), and Nanometrics Trillium 240 (T-240) instruments. (2) It includes a wide-band pressure sensor: either a differential pressure gauge (DPG) or an absolute pressure gauge (APG). (3) All four components of the BBOBS recorded data at a sample rate of at least 5 samples-per-second (sps). Our study does not constitute a quantification of overall data quality; we do not account for station dropouts, broken channels or instrument return rate. We focus on data that are considered ‘good’ to offer an analysis of noise properties that are representative of normal BBOBS operations.

3.2 Data selection and processing

To investigate the relationship of the noise characteristics of BBOBSs with deployment and instrument properties, we select a subset of data at each station from which to calculate power spectra, cross-component coherence, admittance and phase spectra, which make up the transfer functions used for noise corrections (Crawford & Webb 2000; Bell *et al.* 2015). We examine 25 d of data that are not significantly contaminated by earthquake signals, instrument glitches or other transient signals at each BBOBS using the ATaCR code package (Janiszewski *et al.* 2019). These days are randomly distributed throughout each deployment to average across any long-term drift, instrument releveling or seasonal variability (Bell *et al.*

2015; Stähler *et al.* 2016). For all seismometer and DPG channels, we remove the instrument response using a high pass filter with a corner frequency of 1000 s. The response is not removed from APG channels, but we filter the data using the same procedure. All data are downsampled to 5 sps using an anti-alias filter with a corner frequency of 1.25 Hz.

We window each day of data into 16, 7200-s segments, overlapping by 30 per cent, and apply a flat-Hanning taper to the windows. We calculate the auto- and cross-power spectral density functions from the finite Fourier transforms of the time-series (Bendat & Piersol 2010; Bell *et al.* 2015) for each of the 16 windows. Any windows that contain transient signals identified via quality control procedures (see Janiszewski *et al.* 2019 for details) are discarded; if more than 6 windows are discarded, the entire day is rejected and not counted towards the 25-d sample. The windows are subsequently averaged to calculate spectral density functions for each day of data.

We then calculate deployment-average spectral functions for each station by averaging over all windows. A second quality-control step discards individual days that significantly (at 95 per cent confidence level) increase the standard deviation of the noise properties (Janiszewski *et al.* 2019). This avoids the inclusion of days that are dominated by anomalous signals unrepresentative of normal station noise. While this processing procedure may not capture the full range of variability and discards malfunctioning data segments, it is appropriate for examining systematic trends at functioning BBOBSs. For analysis and comparison, we take full-octave averages of the spectra in $\frac{1}{8}$ octave intervals following the procedure of McNamara & Buland (2004). We visually inspect all averaged spectra and discard any that contain data dropouts, flatlined or obviously non-functioning instruments, or instruments where the secondary microseism peak was not visible (e.g. anomalously high noise floor). This results in average spectra for vertical (Z), horizontal ($H1$, $H2$ or collectively H) and pressure (P) components at each BBOBS, as well as average cross-component coherence, admittance, and phase functions.

Finally, we use the computed transfer functions to estimate average tilt- and compliance-corrected Z spectra for each BBOBS (Crawford & Webb 2000). In our discussion, we use Z -corrected to refer to the Z component where both tilt and compliance noise have been removed. To compute the Z -corrected spectra, all four components of a BBOBS must pass the aforementioned quality control procedures. After quality controls, we are left with data from 551 BBOBS with waveforms archived in the IRIS DMC that had at least one component, and 404 that have all four components. This includes instruments from 18 seismic experiments, with deployment years ranging from 2005 to 2019 (Table S1). In calculating the transfer functions, we also calculate the cross spectral properties: the coherence, admittance and phase (Bell *et al.* 2015). Of these, coherence is the simplest to interpret since it varies between zero and one and does not reflect discrepancies in instrument gain or polarity. High coherence between the vertical and pressure components at long periods indicates the presence of compliance noise, and high coherence between the vertical and horizontal components indicates tilt noise (Crawford & Webb 2000). High vertical-pressure coherence also occurs within the microseism band, particularly near the secondary microseism. We analyse the coherences in order to constrain variability in the properties of tilt and compliance noise on the BBOBS.

The approach of Crawford & Webb (2000) scales the transfer function with the coherence; that is, a larger noise removal in the data will occur in locations with higher coherence values. Traditionally, tilt- and compliance-corrections are only calculated

at frequencies <0.1 Hz; another approach is to only calculate corrections in frequency ranges where the coherence between components is above a cut-off value (Bell *et al.* 2015; Tian & Ritzwoller 2017). High coherences are also often observed in the secondary microseism band, and this transfer function correction approach has been extended to these higher frequencies with success (e.g. Bowden *et al.* 2016). Since our investigations only rely on a systematic estimate of noise reduction after corrections, we calculate the corrections following Crawford & Webb (2000) across the entire frequency band, rather than exclude lower-coherence frequency ranges altogether. This may lead to a slightly higher estimate of noise reduction at frequencies with low coherence (in cases where, in practice, it may be prudent to exclude these frequency ranges from the noise removal process), but the effect should be minimal. In addition, users of BBOBS data should be cautious of potential distortion of time-series or amplitude errors when applying corrections systematically over the entire frequency band. A frequency bandwidth-limited removal or an approach that accounts for distortion may be required for some use cases, particularly when the amplitude of the transfer function for water noise and seismic waves is similar. A more detailed discussion can be found in Bell *et al.* (2015).

3.3 Metadata compilation

To compare the noise with instrument and deployment properties, we compile metadata information for all stations in our data set. Instrument design was obtained from the IRIS DMC, and verified through review of individual cruise reports. Instruments are designed by one of the three centres that comprised OBSIP—the Lamont Doherty Earth Observatory (LDEO), Scripps Institute of Oceanography (SIO) and Woods Hole Oceanographic Institution (WHOI). We classify each instrument among eight unique designs according to differences in the seismometer, pressure gauge, or the overall package in which the instruments are housed. We do not attempt to distinguish between upgrades in datalogger versions within a given instrument design. While we utilize manufacturer nomenclature (CMG-3T, T-Compact and T-240) in categorizing seismometers, key seismometer components (levelling system and pressure case) are provided by the instrument operator in most cases. For all designs, we utilize the instrument responses archived with the data at the IRIS DMC. Our categorizations mirror those given in the OBSIP Final Report (Aderhold *et al.* 2019); however, we additionally distinguish between LDEO broad-band instruments that were deployed with either a DPG or an APG. We also include information about the geographic environment of the instruments, which includes ocean basins and marginal seas as defined by the International Hydrographic Organization (1953). The deployments were predominantly located in the Pacific Ocean and its marginal seas, but also include the Atlantic Ocean and Lake Malawi. Details for our instrument design categorization are given in Table 1, and the frequency distributions of these parameters are shown in Fig. S1. We also record the experiment in which each BBOBS was deployed.

We query the water depth of each station from the IRIS DMC; these values are reported by cruise logs, typically from sonar readings at the deployment location or through acoustic ranging (Russell *et al.* 2019), and are typically accurate to ~ 10 m. Where possible, we determine the following geographic properties for each instrument using global compilations: the distance to the nearest land, the distance to the nearest tectonic plate boundary, the age of the underlying oceanic crust, the sediment thickness beneath each BBOBS

and the mean annual surface current velocity. To determine the distance to coastline, we calculate the distance to the nearest major landmass from each station using the data set of Lee *et al.* (2018). This parametrization ignores small islands, as we are most interested in the relationship between noise sources that may arise from ocean-shelf interactions. We calculate the distance to the nearest plate boundary using the compilation of Bird (2003).

We estimate crustal age using the 2-arcmin resolution seafloor age map from Müller *et al.* (2008), which is primarily constrained by prominent marine magnetic anomalies. We use the GlobSed model (Straume *et al.* 2019), a 5-arcmin total sediment thickness grid for the world's oceans and marginal seas, to estimate sediment thickness. We compute mean annual surface current velocity estimates using the near-surface velocity climatology data from the Global Drifter Program (Laurindo *et al.* 2017). For all three data sets, we estimate the variable at the BBOBS by extracting the geographic grid point that overlaps with the site location. If this did not exist, no value was assigned. In total, we compile and examine 11 metadata parameters at each BBOBS: 'Experiment', 'Instrument Design', 'Seismometer', 'Pressure Gauge', 'Environment', 'Water Depth', 'Distance from Land', 'Distance to Plate Boundary', 'Surface Current', 'Sediment Thickness' and 'Crustal Age' (Table S2). The distributions for these parameters are shown in Fig. S2.

There are limitations to our sampling of metadata in this analysis. Many investigated parameters are not evenly distributed. For example, the maximum value for distance to the coastline is 4020 km, but >75 per cent of stations have values less than 1000 km. Some parameters do not have available values for all stations. For example, oceanic crustal age estimates do not exist for stations located on the continental shelves, on submerged Zealandia continental crust, and for lacustrine stations.

3.4 Spectral angle calculation and analysis

A primary goal of this study is to determine the properties (i.e. metadata) of a BBOBS that determine its noise characteristics. To this end, we divide the data set of station spectra into subgroups defined by metadata parameter(s), and then quantify the similarity of spectra within each subgroup. If a certain parameter is highly determinative of noise, then spectra within each subgroup defined by that parameter should be similar to each other, but quite distinct from spectra in the other subgroups.

We use the 'spectral angle' to quantify the (dis)similarity of spectra. This metric accounts for differences in the shape, but not absolute amplitudes, of stations' spectra (e.g. Sohn & Rebello 2002; Wan *et al.* 2002). We are primarily interested in variations in sources of noise (e.g. changes in the frequency distribution and extrema of different noise peaks and troughs), and not in an average noise-level metric. The spectral angle is better suited to this than other metrics we tested (e.g. the Euclidean distance) that are overly sensitive to absolute amplitude. Spectral angle is also diagnostic of differences in noise floor between instruments, due to differences in curvature of the spectra between high noise peaks.

For a given pair of spectra, s_i and s_j , the spectral angle is computed in log-frequency space as

$$\theta_{i,j} = \cos^{-1} \left(\frac{s_i \cdot s_j}{|s_i| |s_j|} \right). \quad (1)$$

We assign a penalty to each individual spectrum, defined as the root-mean-square of its spectral angle with all other spectra in its

Table 1. Information related to different BBOBS instrument types included in this study, including defined abbreviations to distinguish them.

Abbreviation	Design institution	Seismometer	Pressure gauge	Shielding	Instrument name
AB	SIO	T-Compact	DPG	Syntactic foam	Abalone
B2	SIO	T-240	DPG	None	SIO Unshielded Broadband
BA	LDEO	T-Compact	APG	None	LDEO Unshielded APG Broadband
BD	LDEO	T-Compact	DPG	None	LDEO Unshielded DPG Broadband
TRM	LDEO	T-Compact	APG	Steel Plates	LDEO Trawl Resistant Mount OBS
AR	WHOI	T-Compact	DPG	None	WHOI ARRA
BG	WHOI	CMG-3T	DPG	None	WHOI BBOBS
KE	WHOI	CMG-3T	DPG	None	WHOI KECK ¹

Note: 1. The WHOI KECK also includes a strong-motion accelerometer distinguishing it from the WHOI BBOBS.

subgroup:

$$p_i = \sqrt{\frac{1}{n-1} \sum_{j \neq i} \theta_{i,j}^2}, \quad (2)$$

where n is the number of spectra in the subgroup. We then calculate the summed penalty for each subgroup, describing mean spectral similarity, as the sum of the individual stations' penalties:

$$P = \sum_i^n p_i. \quad (3)$$

Finally, the overall penalty function for a given subgrouping scheme is the sum across all subgroups' penalties.

Since the effect of noise is expected to differ between the Z , $H1$ and $H2$, and Z -corrected components, we examine each of these independently. For consistency, we only analyse the 404 instruments with four components that passed quality control. Since the BBOBSs are randomly oriented on the seafloor, we treat the $H1$ and $H2$ components as two representations of the horizontal noise, giving 808 spectra for this H component.

To start, we calculate three total penalties for the entire group of BBOBSs described above (for Z , Z -corrected and H components). This yields a baseline measure of spectral dissimilarity amongst all stations in the data set. We then systematically divide the data set into subgroups of stations defined by each metadata parameter. For example, we use the 'seismometer' metadata parameter to construct three subgroups of noise spectra defined by the parameter's three categorical subdivisions: T-240 s, CMG-3Ts and T-Compacts. We calculate a penalty for each of the k subgroups, P_k , as above, and a total penalty, P , as the summation of the three subgroup penalties. This is done for each seismic component Z , H and Z -corrected, in turn. In general, N in each subgroup varies with our choice of metadata parameter, as discussed below. Subgroups with zero or one station are excluded from the penalty calculation. The larger the reduction in overall penalty function when stations are subdivided according to a given metadata parameter, the more closely linked that parameter is to noise spectral shape.

The metadata parameters we use to subdivide the spectra fall into one of three types: (1) categorical, (2) numerical and (3) incomplete-numerical. For categorical parameters, we use one subgroup for each category. For numerical parameters, we utilize two subgroups, separated by a cut-off value. We determine the optimal threshold value by grid searching to obtain the cut-off that yields the two most internally similar subgroups. Finally, for the numerical variables that lack some data entries (i.e. semi-numerical; Figs S2b, d and f), we place stations lacking numerical values into a separate subgroup,

and use the grid-search approach for numerical parameters for the remaining stations, yielding three subgroups.

Since multiple parameters influence the noise spectra, the subgrouping scheme uses a hierarchical framework. First, we perform the above analysis for each individual metadata parameter. We refer to such single-parameter subgroups as a '1-layer' analysis. For parameters that result in relatively high levels of penalty reduction, we then test the effect of producing additional subgroups by repeating this procedure two times, resulting in a '3-layer' analysis. In all cases, we evaluate success by computing the penalty reduction value, which compares the summed penalty to the baseline penalty.

4 RESULTS

4.1 Average noise spectra

We present average power spectra for each BBOBS seismometer component in Fig. 3. The Z component data are, on average, between the New High and Low Noise Model (NHNM and NLNM; Peterson 1993). As expected, the H components have higher values, above or near the NHNM at all frequencies. At frequencies lower than ~ 0.1 Hz, the H components are on average ~ 20 – 35 dB noisier than the vertical components, likely due to bottom-current noise (Webb 1998). The difference between components is less pronounced at shorter periods. Both the secondary and primary microseism are observed as clear peaks at ~ 0.14 and ~ 0.07 Hz, respectively, where the secondary peak is on average higher than the primary. However, the greatest variability between the spectra is observed in the primary microseism band on both the Z and H components. At frequencies < 0.05 Hz, the infragravity signal manifests as an additional peak on a subset of the vertical spectra. This peak is not observed on the horizontal components since it is drowned out by the stronger bottom-current noise. We also examined the pressure spectra; however, significant variability between experiments suggests a possible instrumentation or gain error for subsets of BBOBSs. Pressure gauge response functions can be prone to calibration error, although the cited variability is typically less than the order of magnitude observed here (Yang *et al.* 2012; Doran *et al.* 2019). At least one of the apparently anomalous pressure spectra is related to an error in the AACSE data that has since been reported and resolved in the IRIS DMC (Figs S5 and S6). We note, however, that gain errors do not affect our ability to perform compliance removal, or interpret coherence or phase information between the Z and P components.

As predicted, for the Z -corrected components, we observe a reduction in noise across all frequencies after the transfer function

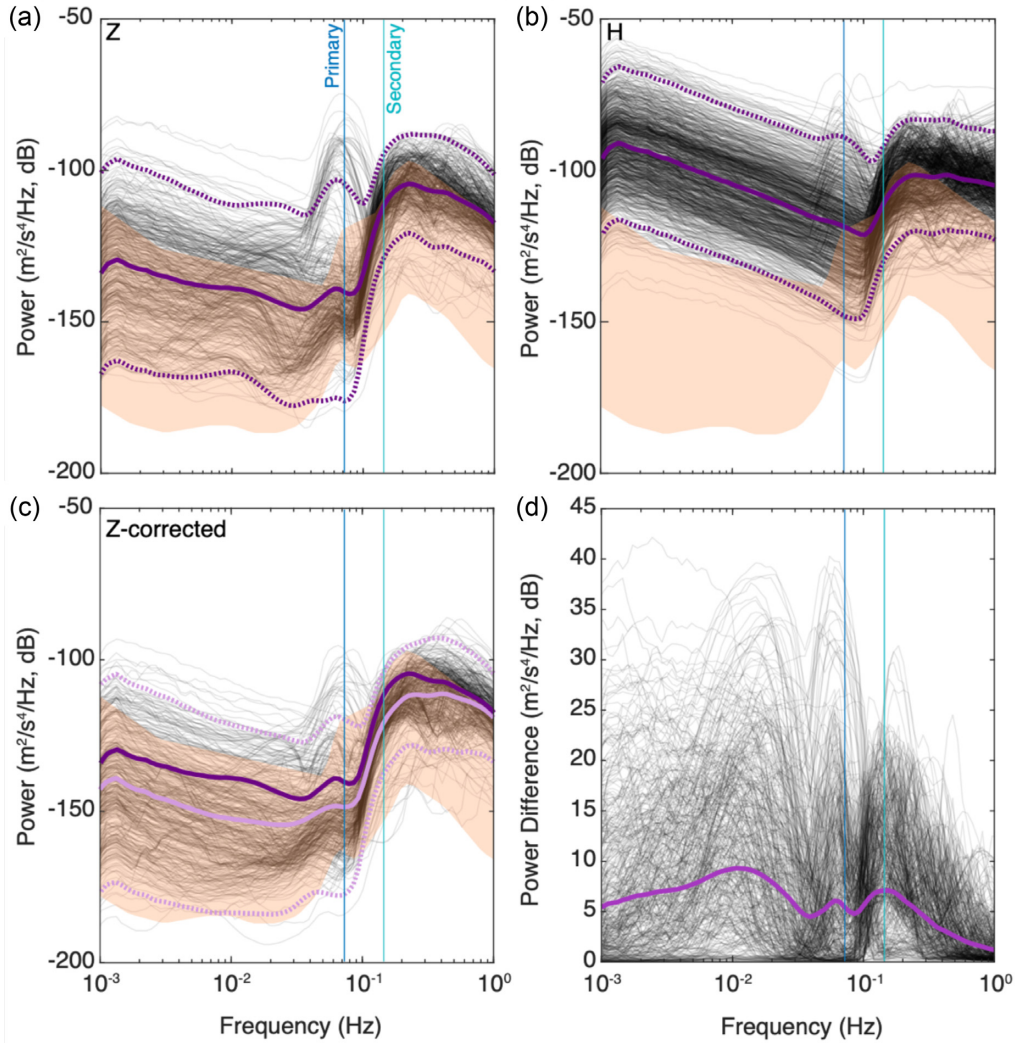


Figure 3. Power spectra for (a) Z , (b) H and (c) Z -corrected for all individual stations plotted as thin black lines. Solid and dashed dark blue lines indicate mean and 2σ standard deviations, respectively, where dark purple indicates the original Z and H spectra (a and b), and light purple indicates the Z -corrected spectra (c). The Z spectra is plotted on (c) for comparison. The Peterson (1993) high and low noise ranges are shown as the orange shaded area. (d) Difference between the Z and Z -corrected spectra; positive values indicate lower values for the corrected data set. The purple line indicates the mean difference. The global primary and secondary microseism peaks are plotted as thin blue lines for reference.

corrections were applied. On average, the corrected spectra are ~ 5 – 10 dB quieter than the original, but reductions as large as ~ 40 dB are observed. Maximal noise reduction is observed at ~ 0.01 , 0.07 and 0.14 Hz, corresponding to tilt and compliance, the primary microseism, and the secondary microseism, respectively (Fig. 3d). We test the order of corrections, comparing the final spectra when compliance is removed after tilt noise versus when tilt noise is removed after compliance noise. To first order, no difference is observed, and for the remaining analyses, Z -corrected spectra are calculated by first removing tilt and then compliance noise. The spectra for the seismic and pressure components grouped by experiment are shown on Figs S3–S7.

4.2 Average coherences

For all BBOBS, we present the coherences between each horizontal and the vertical component, $H1-Z$ and $H2-Z$, and the coherence between the pressure and vertical components, $P-Z$ (Figs 4a–c). On

the $H1-Z$ and $H2-Z$ pairs, we clearly observe high coherence values on a subset of the instruments at frequencies <0.1 Hz with no clear dependence on water depth. This is consistent with tilt noise on the Z component. We observe high $P-Z$ coherence with a water-depth-dependent high frequency limit that agrees with the predicted cut-off for infragravity waves. This is consistent with compliance noise on the Z component. We also observe a region of high $P-Z$ coherence at frequencies at and just above ~ 0.14 Hz, consistent with the secondary microseism. Another, more moderate, peak observed at ~ 0.07 Hz is consistent with the primary microseism. We recalculate the $H1-Z$ and $H2-Z$ coherences after compliance noise removal, and the $P-Z$ coherence after tilt noise removal from the Z component (Figs 4d–f). Since tilt is typically assumed to be the larger noise source, we expect its removal should result in a more visible compliance signal, and an increase in $P-Z$ coherence. As anticipated, we observe that the $P-Z$ coherence tends to increase after the removal of tilt noise at frequencies below the infragravity cut-off. However, we also observe an increase in the $H1-Z$ and $H2-Z$ coherences for some instruments when we first remove the

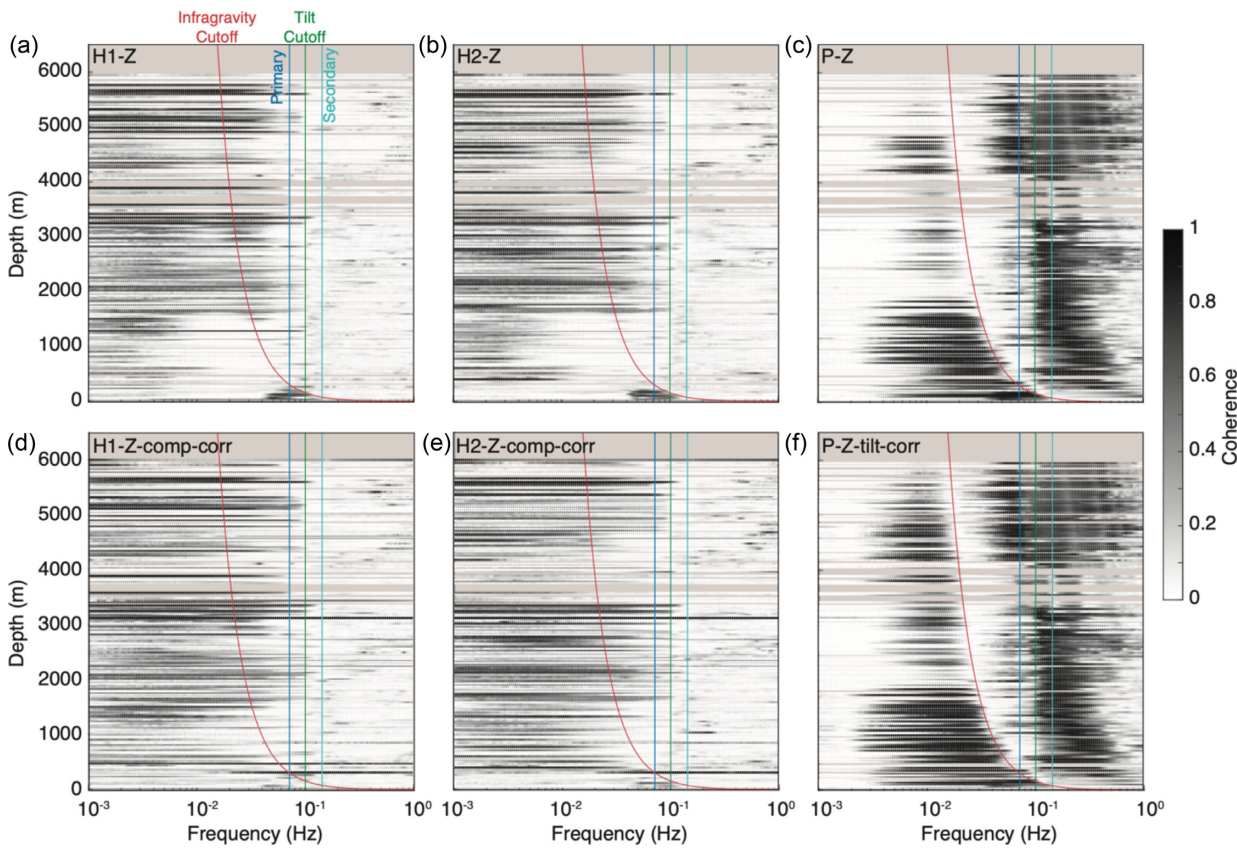


Figure 4. Coherences of the $H1$, $H2$ and P with the Z for each BBOBS compared with the water depth of the instrument. The red line indicates the predicted infragravity cut-off frequency (f) as a function of water depth (d), using the equation $f = \sqrt{\frac{g}{2\pi d}}$ (Bell *et al.* 2015); the green, dark blue and light blue lines indicate the tilt cut-off (0.1 Hz), primary (0.07 Hz) and secondary (0.14 Hz) microseism peaks respectively. (a–c) Coherences calculated with the Z component; (d–e) $H1$ - Z and $H2$ - Z coherences with the Z -compliance-corrected component; (f) P - Z coherence with the Z -tilt-corrected component.

compliance noise. This suggests that the two noise sources may have similar amplitudes at some stations, in contrast to the assumption that tilt noise is typically a much larger noise source (Bell *et al.* 2015). This is discussed further in Section 5.1.

Coherences between horizontal and pressure component pairs are typically not investigated for BBOBS noise characterization and removal, as incoherence is predicted (Crawford & Webb 2000). We mostly observed $H1$ - P and $H2$ - P incoherence in our compiled data set, with the exception of the shallowest stations, where coherences were >0.5 near 0.1 Hz for both these component pairs (Fig. S8). Tilt and compliance corrections for the Z component can still be used in this frequency band at these shallow water instruments (Webb & Crawford 2010; An *et al.* 2020), as long as this coherence is accounted for.

4.3 Determinants of station noise

Our systematic calculation of the (dis)similarity between station noise spectra after subdividing stations by each metadata parameter yields quantitative estimates (in terms of ‘penalty’, the measure of dissimilarity) of the relative importance of these features in controlling noise properties. A higher penalty reduction suggests that a given parameter is a better predictor of spectral characteristics. As a baseline, the mean penalty per trace for the Z , Z -corrected and H components is 4.94, 4.27 and 4.46, respectively. We report ‘penalty reduction’ as a per cent deviation from these values.

4.3.1 1-Layer analysis

We first discuss results for our 1-layer analysis (Fig. 5a). The largest penalty reduction is obtained when grouping stations by ‘Experiment’ (a mean penalty reduction of 17.4 per cent, when averaging over the Z , H and Z -corrected components). Next is ‘Instrument Design’, which produced an average penalty reduction of 15.6 per cent, and yields the largest penalty reduction for the Z component (19.8 per cent). However, neither of these parameters directly illuminate the physical processes controlling seismic noise, as they strongly co-vary with other metadata. For example, 14 (out of 18) experiments involve only one type of instrument design and seismometer (Table S1). Experiments typically occupy a small footprint (Fig. 1), so intra-experiment variation in the environment is also limited. Similarly, ‘Instrument Design’ covaries with ‘Seismometer’, ‘Water Depth’ (e.g. TRM designs are only deployed in <1000 m) and ‘Pressure Gauge’. Nonetheless, the significant penalty reduction under these two parameters demonstrates that experiment and instrument parameters collectively have substantial impact on noise characteristics, reinforcing the need for careful deployment planning.

The ‘Seismometer’ parameter has the next greatest influence on the noise spectra (Fig. 5a), reducing the total penalty by ~ 10 per cent for both Z and H components. For the Z component, the ‘Seismometer’ subgroup spectra show different signatures of classic BBOBS noise (Fig. 6). The sensor packages containing CMG-3Ts display a power law (linear in log–log space) amplitude increase at

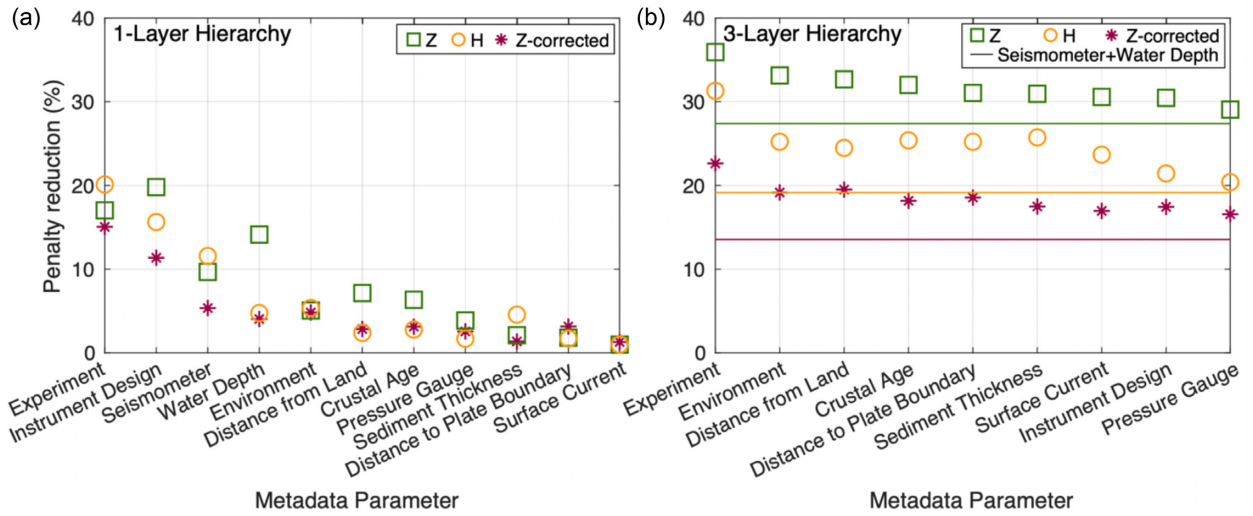


Figure 5. Percentage penalty reduction in spectral angle for Z , H and Z -corrected for each metadata parameter subdivision. Larger reductions indicate more similarity within the final subgroups. Parameters are sorted from left to right in descending order of their average penalty reductions. (a) Results for each metadata parameter (1-layer analysis). (b) Results after subgrouping the BBOBS by ‘Seismometer’, then ‘Water Depth’, and then the labelled metadata parameter (3-layer analysis). The 2-layer penalty reductions for ‘Seismometer’ and ‘Water Depth’ are shown by the solid lines.

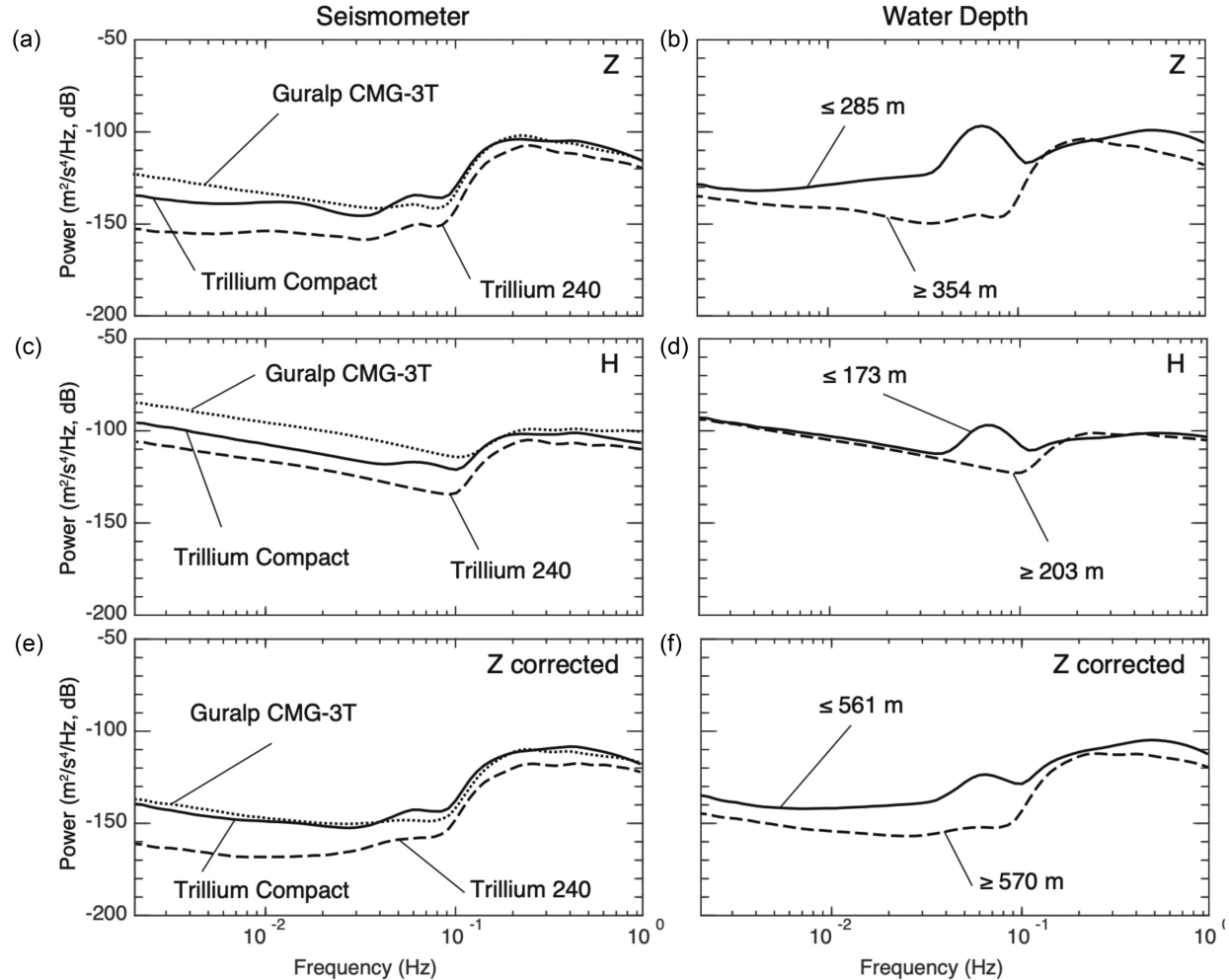


Figure 6. Average spectra calculated from the resultant metadata subgroups based on ‘Seismometer’ and ‘Water Depth’. (a) The average Z spectra for the three ‘Seismometer’ subgroups: CMG-3T, T-Compact and T-240. (b) The average Z spectra for the two ‘Water Depth’ subgroups (grid search determined cut-off depths indicated). (c) Same as (a), but for the H components. (d) Same as (b), but for the H components. (e) Same as (a), but for the Z -corrected component. (f) Same as (b), but for the Z -corrected component.

frequencies below 0.1 Hz, characteristic of tilt noise. By contrast, sensors containing T-240 s and T-Compacts have more spectral curvature and multiple inflection points at the same low frequencies, which is characteristic of compliance noise (Bell *et al.* 2015). The *H* spectra provide further insight (Fig. 6c). All three seismometer subgroups show bottom current noise (an \sim 18 dB Hz $^{-1}$ -decade linear increase in log–log space at low frequencies). However, the subgroups of *H* spectra are clearly distinguished by their noise notch relative to their secondary microseism peak. The CMG-3Ts have the least distinct noise notch (just \sim 15 dB below the secondary microseism), and are the noisiest instruments, on average, at long periods, especially for horizontals. T-Compacts have an intermediate noise notch (\sim 20 dB below the secondary microseism), partially influenced by the substantial primary microseism associated with shallow water shielded instruments. T-240 s have a noise notch \sim 30 dB below the secondary microseism, and have the quietest horizontals at long periods. The average spectra for the *Z-corrected* components for the CMG-3Ts and the T-Compacts are nearly identical; however, long period noise on the T-240 s remains \sim 20 dB quieter (Fig. 6e).

In the higher-frequency band (0.1–1 Hz) dominated by the secondary microseism, the T-240 s peak \sim 10 dB lower than the other sensors, on all components. This observation is somewhat surprising, as the secondary microseism peak is ubiquitous in all ocean environments and does not vary dramatically even with depth (Fig. 6). We have considered the possibility that incorrect instrument gain(s) may contribute to this apparent offset (Doran & Laske 2019), and tested the potential impact of this error on our results by adding a constant 10 dB to spectra that have an anomalously low secondary microseism peak. The overriding conclusion of our tests is that the quantitative subgroupings and associated interpretations are not sensitive to gain uncertainty of this magnitude, but this may slightly impact the absolute amplitude differences observed between different seismometer packages. We discuss these metadata uncertainties further below.

'Water Depth' has a similar level of influence on the noise spectra as the '*Seismometer*' parameter. These two categories are also parsimonious in their numbers of subgroups (2 and 3, respectively). '*Water Depth*' is particularly deterministic for *Z* component noise, with a penalty reduction of 14.1 per cent, compared to 4.8 per cent for *H*, and 4.0 per cent for *Z-corrected* (Fig. 5). Unlike for the '*Seismometer*' parameter, '*Water Depth*' subgroups were determined by grid search. The cut-off depths separating these subgroups are relatively shallow for all three components, between \sim 200 and 500 m depth. This cut-off separates shallow versus deep noise environments, reflecting the distinctive signal of shallow water infragravity waves in the 0.04–0.1 Hz band, likely due to direct wave loading that overlaps with primary microseism frequencies, observed on all components (Webb & Crawford 2010; An *et al.* 2021). Our depth resolution is limited by the depths at which BBOBS were deployed; thus, we report the maximum and minimum depths of the shallow and deep subgroups, respectively (Fig. 6). While this shallow water signal is present on all components, compliance noise continues to influence the *Z* component at lower frequencies (<0.03 Hz), following the characteristic depth dependence of infragravity waves (Fig. 4). This explains the greater penalty reduction for the *Z* component, relative to the *H* and *Z-corrected* components. A more detailed investigation of the grid search for the *Z* component indicates two depths where there are sharp changes in the penalty function: (1) the 200–500 m cut-off discussed above and (2) an inflection at \sim 2600 m water depth (Fig. S9). This may reflect the variable frequencies of the compliance noise, and suggests broadly that categorization into

shallow, mid-depths and deep-water regimes is useful for predicting overall BBOBS noise levels for a deployment.

The remaining parameters are less useful singular determinants of noise characteristics, as they mostly have smaller penalty reductions (<5 per cent for each component). The penalty reductions for the *Z* component using '*Crustal Age*' and '*Distance from Land*' are somewhat higher; however, covariance with '*Water Depth*' likely explains this observation. Covariance amongst parameters is exemplified by the apparently perverse observation that '*Pressure Gauge*' has some apparent predictive power for the noise characteristics of the seismic components.

4.3.2 3-Layer analysis

For the 1-layer analysis, the power of any single parameter to predict noise characteristics is limited, with 6.5 per cent of variation explained, on average. This low value indicates the multifactorial controls on BBOBS noise. Therefore, we expand our analysis up to three layers to determine which combinations of parameters yield subgroupings with the most similar spectral characteristics. This also helps us test which parameters (if any) have a secondary role in regulating noise variability.

We start with a new baseline 2-layer analysis. We group stations by '*Seismometer*' (three subgroups), and then by '*Water Depth*' (two subgroups), yielding a total of six subgroups (Fig. 7). These two parameters were chosen on the basis of their high penalty reduction (Section 4.3.1), their parsimonious subgroups, their relative lack of covariance with simpler parameters, and their clear physical relationships with noise, facilitating interpretation. The 2-layer analysis yielded a 20 per cent average penalty reduction (horizontal lines in Fig. 5b), with 27.4 per cent for the *Z* component, 19.2 per cent for the *H* components, and 13.5 per cent for *Z-corrected*. As above, the larger penalty reduction for the *Z* component reflects its sensitivity to both compliance and tilt. This is further supported by the relatively low penalty reduction (i.e. higher intergroup similarity) for the corrected vertical component (*Z-corrected*), which nominally has these effects removed. On the other hand, the fact that the *Z-corrected* component still has non-zero penalty reduction demonstrates that factors other than tilt and compliance influence noise characteristics, or that these corrections do not work perfectly. More sophisticated methods of noise removal, such as algorithms that account for temporal variability of the transfer functions, or iterative removal processes (Bell *et al.* 2015; Tian & Ritzwoller 2017), might drive this '*Z-corrected*' penalty reduction down further.

We conducted independent grid searches for water depth cut-off values in each seismometer subgroup. The optimal depth cut-off for the T-Compact subgroup was between 354 and 430 m, very similar to the shallow cut-off depths discussed above (Fig. 7). T-Compact seismometers are used in the majority of the shielded BBOBS instruments designed for shallow water deployments <1000 m. By contrast, the T-240 and CMG-3T subgroups have deeper apparent cut-offs, between 2564–2687 m and 2785–2822 m, respectively. This is similar to the secondary mid-depth cut-off noted above. Since these subgroups do not include most of the shallow-water BBOBS, they do not include characteristically very shallow (<500 m depth) spectra, and so their intragroup grid searches find what we believe to be an important local minimum in penalty at \sim 2600 m. Close investigation of the grid search results for the Trillium Compacts (Fig. S9) reveals the same local inflection at \sim 2600 m cut-off depth.

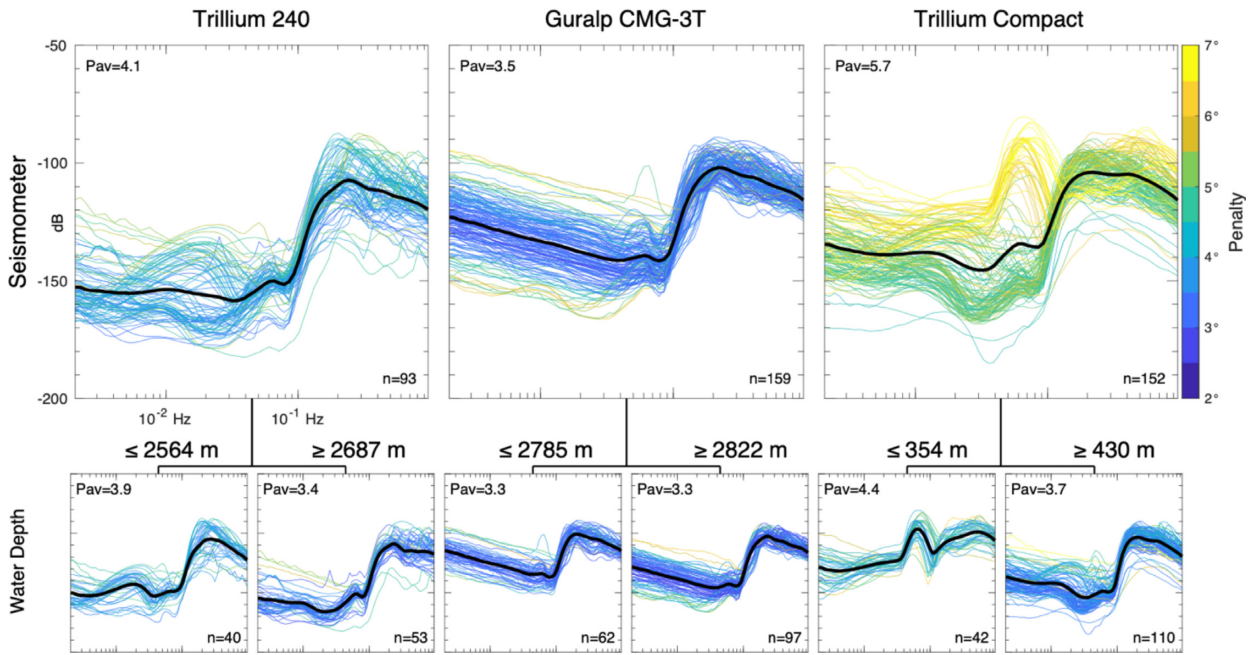


Figure 7. Example of subgrouping by spectral similarity, showing the 2-layer analysis for Z spectra. These were first subgrouped by ‘Seismometer’, then subgrouped by ‘Water Depth’. The seismometer types and threshold depths are indicated above each plotted subgroup. For each subgroup, the average spectrum is plotted in black. Individual spectra are coloured according to their average spectral angle (i.e. penalty) from the other spectra in that subgroup. The same vertical and horizontal scale is used for all plots. The number of spectra (n) and the average penalty (P_{av}) for each subgroup is given in the corresponding plots.

Finally, we perform a 3-layer analysis. Each of the six subgroups from the 2-layer ‘Seismometer’ and ‘Water Depth’ analysis is further subdivided according to each of the remaining parameters (e.g. Figs 7, S10–12), and penalty reduction is measured. Aside from ‘Experiment’ (see caveats below), ‘Environment’ yields the highest 3-layer penalty reduction (25.8 per cent mean reduction, or 5.8 per cent above the 2-layer baseline, for all components). This is likely explained by differences in the frequency distribution of the secondary microseism across ocean basins (Babcock *et al.* 1994; Yang *et al.* 2012). ‘Distance from Land’ is the numerical parameter that provided the highest penalty reduction, approximately 5.5 per cent above the 2-layer baseline for all components. While not included in the main analysis, we test the effects of including ‘Water Depth’ again in the third layer. It results in similar penalty reductions as ‘Distance from Land’, which is likely a consequence of covariance between water depth and distance from land.

Other numerical parameters in the 3-layer analysis yield lower penalty reduction, but all improve upon the 2-layer baseline by $>\sim 3$ per cent. The fact that several, rather than any one, of these parameters control noise characteristics is highlighted by the particularly high penalty reduction (9.9 per cent above the 2-layer baseline across components) for ‘Experiment’ in the 3-layer analysis. As discussed above, because individual experiments do not usually span large portions of metadata space, this parameter effectively combines many other parameters. Thus, it functions as a heuristic for the extent to which station noise is determined by all the station metadata collectively. One way of looking at this is as a lower bound for the aspects of station noise that are deterministically based on instrument type and location, with the remainder of variability owing to random site characteristics and spatiotemporally varying sea state. A final point of note is that moving from the 1- to 3-layer hierarchy, ‘Instrument Design’ switches from providing the second highest to the second lowest penalty reduction. Of course, instrument design is strongly related to seismometer type and—via shielding—water

depth. However, this result indicates that having controlled for covariance with those factors, the design of the instrument is not itself highly impactful on noise characteristics.

4.3.3 Significance of observations

Finally, we consider the possibility that we observe penalty reduction simply by chance. We test the significance of the observed penalty reduction by computing the penalty reduction for 10 000 random subgroups of spectra. In each iteration, we keep the same number of subgroups and number of stations in each subgroup as in the true groupings analysed above. However, instead of assigning stations into each subgroup according to their metadata parameters, we assign them randomly. Taking the example of the 3-layer analysis of ‘Seismometer’, ‘Water Depth’ and ‘Distance from Land’, the random assignments yield a mean penalty per trace of 4.93 (the standard deviation is 0.02, and 95 per cent of the random iterations yield a value above 4.89). This is only a 0.88 per cent penalty reduction from the baseline (of 4.94), compared with the 32.7 per cent penalty reduction when the data are grouped according to real parameters (which is 88 standard deviations removed from the baseline). This analysis establishes the strong significance of the relationships between metadata and station noise characteristics spectra (Fig. S13).

4.4 Frequency and amplitude variability

While the previous analysis focuses on causes of interstation variability in the noise spectra from 0.001 to 1 Hz, most seismic applications of BBOBS data use a band-limited frequency range. We calculate mean noise levels in four commonly used frequency bands. We focus on the following bands: (1) 0.1–1 Hz, centred over the secondary microseism band; (2) 0.05–0.1 Hz, centred over the primary microseism band and traditional noise notch in BBOBS instruments, both of which are relevant for ambient-noise analyses (e.g. Zha *et al.*

2013; Russell *et al.* 2019; Yang *et al.* 2020), teleseismic body-wave imaging (e.g. Wolfe *et al.* 2009; Hawley *et al.* 2016; Eilon & Abers 2017; Bodmer *et al.* 2018), scattered-wave imaging (e.g. Leahy *et al.* 2010; Janiszewski & Abers 2015; Rychert *et al.* 2018; Mark *et al.* 2021) and shear wave splitting (e.g. Collins *et al.* 2012; Eilon *et al.* 2014; Bodmer *et al.* 2015; Lynner & Bodmer 2017); (3) 0.01–0.05 Hz, the primary band for teleseismic long-period body- and surface wave velocity and attenuation imaging (e.g. Weeraratne *et al.* 2007; Tilmann & Dahm 2008; Laske *et al.* 2011; Jin *et al.* 2015; Mazzullo *et al.* 2017; Cai *et al.* 2018; Janiszewski *et al.* 2019) and (4) 0.005–0.01 Hz, of interest for very long-period surface wave (e.g. Lin *et al.* 2016) and normal-mode (e.g. Bécel *et al.* 2011; Deen *et al.* 2017) studies.

Based on the spectral angle analysis in the previous section, we plot noise levels as a function of water depth, parsed according to seismometer and instrument design (Fig. 8). This analysis complements our spectral angle approach by comparing average absolute amplitudes in discrete frequency bands, rather than amplitude-agnostic spectral shape. Fig. 8 illuminates several points that should be considered carefully during experiment design. First, there are no clear trends in noise level as a function of water depth, seismometer or instrument type in the secondary microseism band (0.1–1 Hz). Most BBOBS tend to cluster near the NHNM (Peterson 1993) in this range for both the vertical and horizontal components. Importantly, this is true even for the shallowest BBOBS, as this band is largely above the frequencies at which compliance noise is present. Some instruments display noise levels up to ~ 50 dB quieter on average, but it is possible that instrument-gain uncertainty contributes to these outliers (Doran & Laske 2019).

In the primary microseism band (0.05–0.1 Hz), Z and H component noise levels increase for shallow BBOBS, consistent with direct seafloor loading due to infragravity waves; this effect is reduced for the Z -corrected component, but relatively high noise levels at the shallowest depths persist even after corrections. For each component, shallow water instruments have the highest noise levels in this frequency range.

In the lower frequency bands (<0.05 Hz), the effect of compliance noise, in addition to tilt, is observed on the Z components, evidenced by the dependence on water depth. In contrast, the H components as a whole do not show a clear dependence on water depth in these bands; this may reflect the effectiveness of instrument shielding in mitigating strong shallow seafloor currents, and/or the fact that seafloor currents are pervasive at all ocean depths. The CMG-3T seismometers show a stronger trend of decreasing noise levels with water depth relative to the other seismometers, indicating that this trend may depend on instrumentation; however, further analysis is needed to assess the significance of this observation. The compliance and tilt corrections are generally effective in these bands, and the Z -corrected noise levels are largely distributed between the NLNM and the NHNM.

On average, BBOBS containing T-240 seismometers have the quietest noise levels at all frequency bands, but the differences become more pronounced at lower frequencies. This observation holds even accounting for the possibility of gain errors in some T-240 deployments (Doran & Laske 2019). Importantly, this difference remains after tilt and compliance removal; that is, T-240 sensors have, on average, the quietest Z -corrected components, with many deployments showing noise characteristics just above the NLNM. At frequencies lower than 0.1 Hz, BBOBS that contain a CMG-3T seismometer show higher noise levels than BBOBS with other sensors, particularly on the H components. The exaggeration of

this effect at frequencies lower than 0.1 Hz is consistent with the presence of bottom current and tilt noise.

5 DISCUSSION

Station metadata are strongly predictive of BBOBS noise characteristics. When stations are grouped by metadata parameters, there is substantially more similarity between spectra within those groups compared to the similarity averaged across the whole data set (Figs 5 and 7). The water depth and seismometer type are the two most important factors that determine noise characteristics. The covariance between seismometer and instrument design complicates understanding the relative roles of these two parameters. However, consideration of these results may be useful during experiment design. For instance, if analysis relies upon 0.05–0.1 Hz period teleseismic S - p converted phases to evaluate mantle discontinuities, it is ill-advised to deploy in <500 m water depths, as these signals will likely be dominated by noise that persists after tilt and compliance corrections. Similarly, the CMG-3T seismometer package seem to be the most noise-prone seismometers across a range of environments. Here we further discuss sources of noise, implications for data quality and traditional noise corrections, limitations of our analysis and potential next steps for the BBOBS community.

5.1 Tilt and compliance noise

We have already suggested that the strong link between noise characteristics, and the seismometer and water depth parameters is primarily driven by variations in the tilt and compliance effects, respectively. Here we investigate how coherence between components can illuminate the relative roles of these noise sources as a function of seismometer, water depth, and instrument design. Importantly, the coherence is insensitive to any gain errors. We also discuss how these may affect noise removal approaches.

Compliance noise is characterized by high average P - Z coherence from ~ 0.005 Hz (due to our instrument response removal procedure) up to the theoretical infragravity frequency limit (Crawford & Webb 2000). Fig. 4 shows very good agreement between the high-frequency limit of P - Z coherence and the predicted cut-off frequency at water depths spanning the full range from 0 to 6000 m. Unsurprisingly, water depth is a primary factor in determining a station's compliance noise signature.

We estimate the presence of tilt noise from the maximum average coherence (in the range 0.005–0.035 Hz) between the $H1$ - Z and $H2$ - Z components. We follow the method of Bell *et al.* (2015), grid searching through horizontal component azimuths to find the orientation (theoretically the physical tilt direction) that gives the maximum coherence with the vertical (H_{tilt}). Based on investigations of only the first year of Cascadia Initiative data, Bell *et al.* (2015) suggested systematically higher tilt noise on the CMG-3T seismometer systems, and that the tilt direction on these sensors tended to preferentially align with the $H1$ component. We investigate these properties further using our newly expanded data set.

First, we observe that Z - H_{tilt} coherence is higher on instruments with CMG-3T seismometers (Fig. 9), consistent with a higher propensity for tilt noise (Bell *et al.* 2015). On average, the coherence is ~ 0.8 , above the typical benchmark value used for tilt removal (Bell *et al.* 2015; Tian & Ritzwoller 2017). This higher tilt noise could arise from higher susceptibility of these sensor packages to current noise, and/or a tendency of these instruments to remain slightly out of level (i.e. to have a Z component that is not perfectly

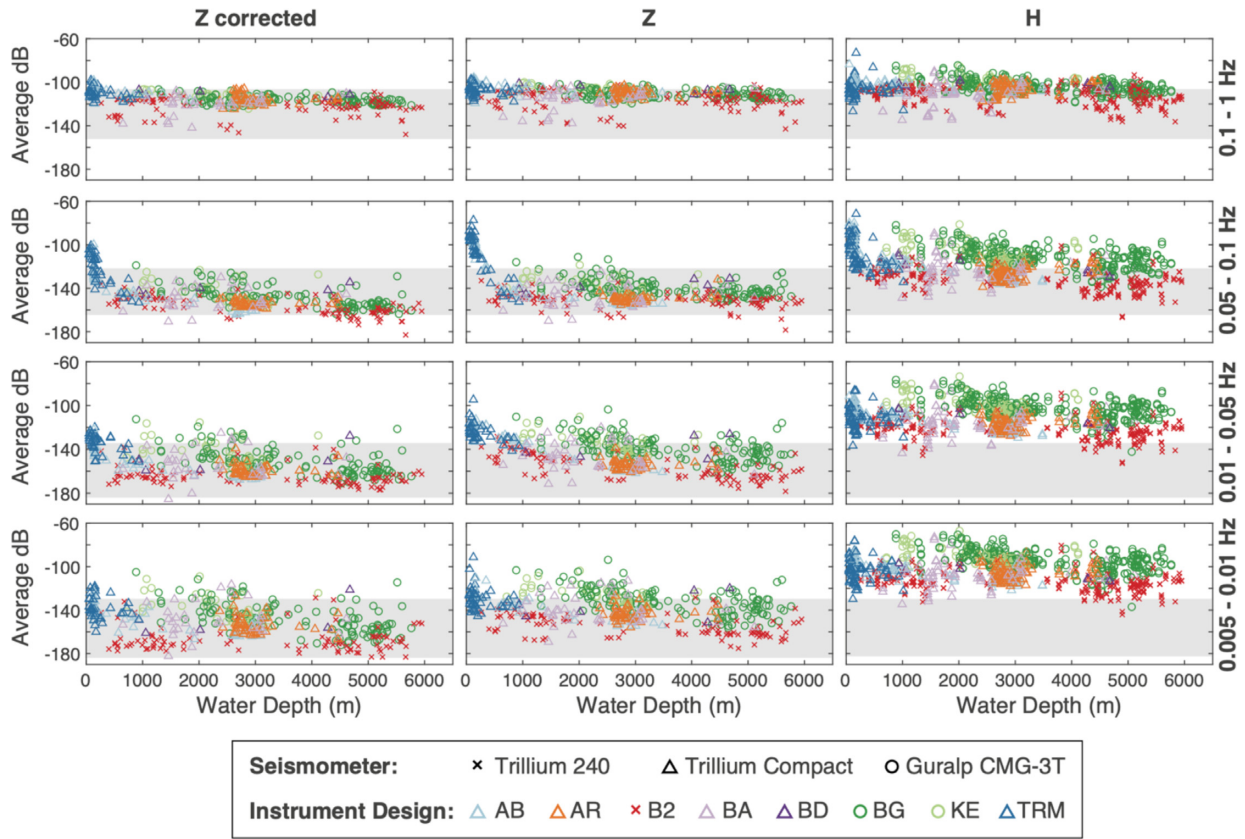


Figure 8. Average power for the Z , H and Z -corrected components plotted as a function of water depth for each BBOBS in four frequency bands (ranges shown on right). Symbols indicate the seismometer; colours indicate the instrument design (see Table 1 for more details). Grey shading indicates the average Peterson (1993) high and low noise model range in each frequency band.

vertical). The analyses in Section 4.3 suggest that a combination of these effects may be important. While all seismometer types show similar low-frequency noise with a log-linear slope below 0.03 Hz on the H components, indicative of bottom current noise, amplitudes are systematically higher on CMG-3T systems (Fig. 6), suggesting that these sensors, and/or the instrument packages housing the sensors, are more strongly impacted directly by currents. In addition, only this seismometer shows this log-linear trend on the Z component (Fig. 6), suggesting that it more commonly transfers current noise into Z -component tilt noise. We observe no systematic tilt direction (Fig. 9), unlike the observations from Bell *et al.* (2015).

In contrast to this high tilt susceptibility, BBOBSs that use either the T-Compacts or T-240 s have mean $Z-H_{\text{tilt}}$ coherences that are <0.5 , lower than typical benchmark values for useful tilt noise removal (Bell *et al.* 2015; Tian & Ritzwoller 2017). The T-Compacts offer the next highest $Z-H_{\text{tilt}}$ coherence after the CMG-3T seismometers; of these, average coherence for the TRM and AB shielded designs is particularly low, supporting the suggestion that shielding protects against horizontal noise contamination. However, unshielded BBOBSs using the T-240 s also have comparably low values, suggesting that these seismometers may simply be less susceptible to tilt noise.

Tilt noise is typically assumed to be higher amplitude than compliance noise, but is not always present. Compliance noise is always present but may be masked by strong tilt noise (Crawford & Webb 2000). It is therefore conventional to first remove tilt noise, which should lead to an increase in the $P-Z$ coherence allowing for subsequent removal of the compliance noise. Our analysis (Fig. 9)

suggests this sequence of noise removal is particularly important for stations with CMG-3Ts. On the other hand, Tian & Ritzwoller (2017) find that both tilt and compliance noise interfere with each other (that is $H1-Z$ and $H2-Z$ coherence increases after compliance removal, and $P-Z$ coherence increases after tilt removal), consistent with relative similarity in their strength. They suggest that multiple iterations of corrections may be appropriate in such cases. To investigate this systematically, we compare the $P-Z$ coherence before and after tilt correction (Fig. 10a), and $H1-Z$ and $H2-Z$ coherences before and after compliance correction (Figs 10b and c). For consistency between the two, we report the average coherence over the frequency range where compliance effects are present, which is inclusive of the range where tilt noise is expected for all stations.

As expected, the $P-Z$ coherence increases for most instruments after tilt noise removal (Fig. 10a), validating conventional noise removal approaches (e.g. Wei *et al.* 2015; Accardo *et al.* 2017; Cai *et al.* 2018; Janiszewski *et al.* 2019). This test also reinforces the predominance of tilt effects on CMG-3T instruments: these seismometers have the largest gains in $P-Z$ coherence, but see essentially no change in compliance-corrected $H1-Z$ or $H2-Z$ coherences (Fig. 10b). In contrast, for instruments with Trillium seismometers, we find increases in both the tilt-corrected $P-Z$ coherence and compliance-corrected $H1-Z$ and $H2-Z$ coherences. This suggests that at individual instruments either the two noise sources are similar in amplitude and interfere with one another, or that in some cases compliance removal may improve the ability to distinguish tilt noise on an instrument. A more detailed analysis of individual instruments is necessary to distinguish between these end member

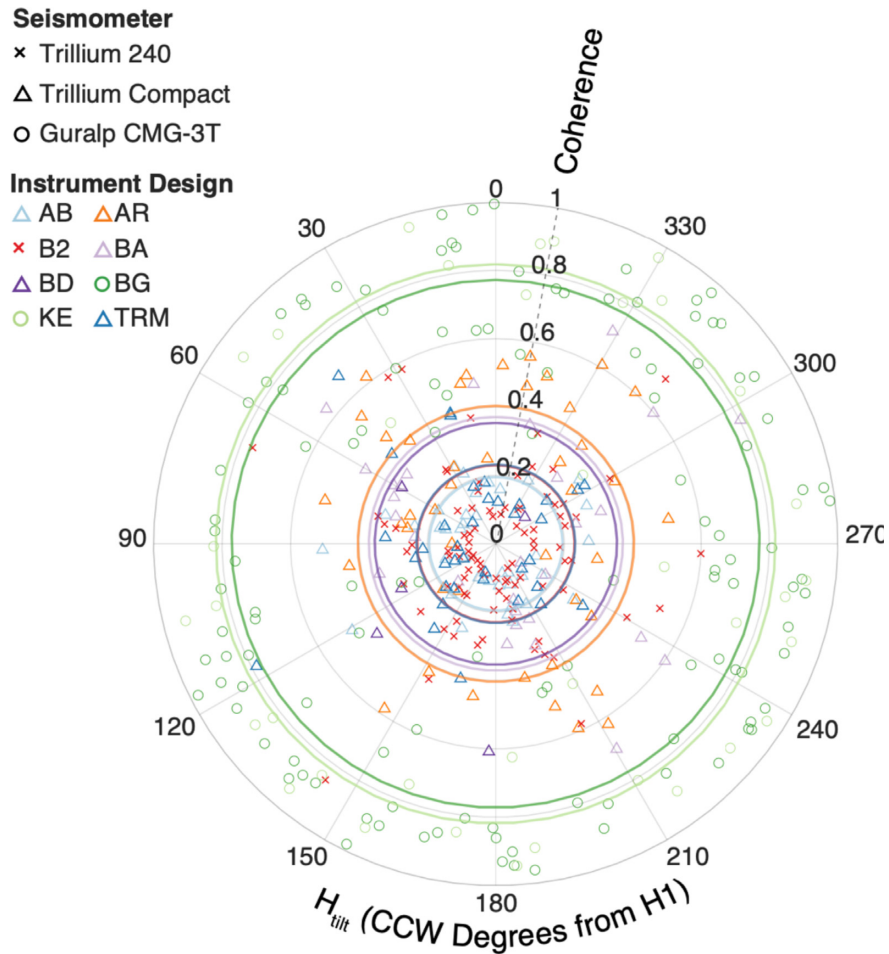


Figure 9. The tilt orientation (H_{tilt}), measured as a function of degrees counter-clockwise from $H1$, and the corresponding $H_{\text{tilt}}\text{-}Z$ coherence for each BBOBS. Symbols and colours indicate seismometer and instrument design. Coloured lines show the average $H_{\text{tilt}}\text{-}Z$ coherence for each instrument design.

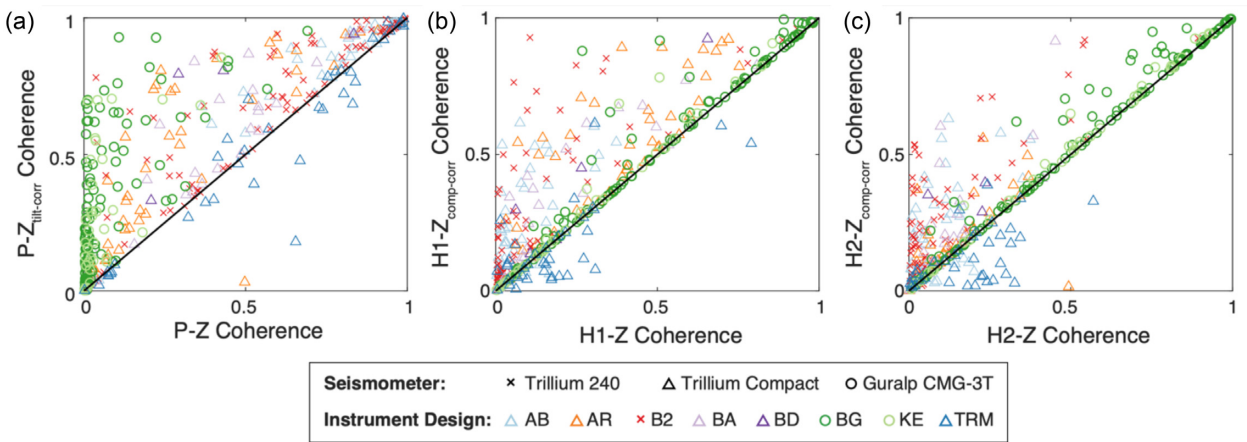


Figure 10. Comparison of coherences before and after tilt or compliance corrections. Symbols and colours indicate seismometer and instrument type; symbols that plot above the black line indicate an increase in coherence after corrections, below the line indicate a decrease in coherence, and along the line indicate no change. (a) Comparison of the $P\text{-}Z$ and $P\text{-}Z\text{-tilt-corrected}$ coherences. (b) Comparison of the $H1\text{-}Z$ and $H1\text{-}Z\text{-compliance-corrected}$ coherences. (c) Comparison of the $H2\text{-}Z$ and $H2\text{-}Z\text{-compliance-corrected}$ coherences.

behaviours. In addition, recalculation of the tilt orientation after compliance removal, and testing of iterative noise removal methods may further help to determine properties and best practices related to the noise and its removal, but is beyond the scope of this study (Tian & Ritzwoller 2017). Furthermore, whether this behaviour remains

stationary throughout the deployment of an instrument remains unclear.

Finally, coherence actually decreases after noise removal at a subset of the TRM and AB instruments (Fig. 10). These instruments have mostly high (>0.5) $P\text{-}Z$ coherences in the expected frequency

range for compliance noise. We reiterate that these instruments also have high $H1\text{-}Z$ and $H2\text{-}Z$ coherences in the primary microseism band (Fig. 4); the lower (<0.5) values observed here stem from averaging over the entire compliance frequency band, which is wider than the microseism. For such a decrease in coherence to occur, the noise across all four components of the BBOBSs must be coherent, which is a property only observed on shallow water instruments. With the exception of one AR instrument that may be affected by an error, all instruments that have a decrease in coherence are deployed in less than 280 m water depth.

5.2 Shallow water instruments

Shallow water BBOBSs have demonstrably distinct noise characteristics (Fig. 6; Webb & Crawford 2010; An *et al.* 2021). Since this is one of the strongest defining characteristics of observed BBOBS noise, here we further investigate if these characteristics are present on all shallow water instruments. Given the set of water depths chosen as the optimal division between shallow and deep instrument noise characteristics (e.g. Section 4.3), we suggest <500 m depth as a conservative limit below which shallow water noise characteristics should be expected. These spectra typically contain a high amplitude peak on all components within the primary microseism band, extending to the predicted infragravity wave cut-off frequency. This peak is reduced, but not removed, by noise corrections (Fig. 6). Within this band, pressure coherence with all seismic components of the BBOBSs is high (Figs 4 and S8) due to both vertical and horizontal loading of the seafloor from ocean waves directly above the instrument (Webb & Crawford 2010).

Only three experiments in our data set deployed instruments at depths <500 m: the Alaska-Aleutians Community Seismic Experiment (AACSE), located offshore Alaska; the Cascadia Initiative (CI), located offshore the northwest coast of the United States; and SEGMeNT, located in Lake Malawi in Africa. The former two share environmental similarities: the continental shelf adjacent to the Pacific Ocean basin. Their noise characteristics are also similar (Fig. S14); the majority of these shallow BBOBSs contain the expected high amplitude peak on vertical and horizontal components at ~ 0.07 Hz. In contrast, this feature is much weaker at the Lake Malawi stations (Fig. S14), which record the primary ocean microseism in the far field. Lake Malawi stations instead manifest a strong noise peak at 0.3–1.6 Hz (Carchedi *et al.* 2022). This is likely due to differences in the characteristic wavelength of wind-driven waves in lacustrine versus oceanic settings. While microseisms are generated at lakes, they have distinctively higher frequencies than those generated in the oceans (Xu *et al.* 2017; Smalls *et al.* 2019) explaining the strong 0.3–1.6 Hz peak (Carchedi *et al.* 2022). Lake infragravity waves are also present (Accardo *et al.* 2017), seen from 0.02 to 0.06 Hz (Fig. S14).

Importantly, these differences may impact the application of different seismic analysis techniques on the data. For example, at Lake Malawi the separation of the ocean microseism from both the lake-generated microseism at higher frequency and lake infragravity waves at lower frequency allowed Accardo *et al.* (2017) to observe clear ambient noise cross-correlation signals between lake-bottom and land seismometers in the 0.04–0.125 Hz range, including at those instruments deployed at depths <500 m. By contrast, ambient noise cross-correlations from shallow-water instruments in Cascadia had low signal-to-noise ratios at these frequencies (Tian & Ritzwoller 2017; Janiszewski *et al.* 2019), due to local ocean-generated waves swamping the microseism signal.

5.3 Limitations

Although this study constitutes the largest systematic review of BBOBS noise characteristics conducted to date, there are important limitations to the data set. Chief among these is that U.S. BBOBS deployments using modern instrumentation have unevenly sampled large swaths of the metadata parameter space. For instance, there is more data from the Pacific Ocean than elsewhere, and a relative paucity of stations atop thick sediments or at great distance from coastlines (Figs S1 and S2). A corollary to this uneven sampling is covariance in several station parameters, which makes it more challenging to tease apart the individual influences of, say, shielding versus shallow water on noise. Although we have attempted to pick apart the most important parameters controlling noise characteristics (Section 4.3), intrinsic covariation makes it impossible to separate parameters completely. This is most clearly seen from Fig. 5 where the ‘Experiment’ is the most important parameter determining noise characteristics, simply because the small geographic footprint of most experiments means that other station parameters are alike within each experiment, and most experiments use a homogeneous instrument design. We also emphasize that certain ‘Instrument Designs’ only use one type of ‘Seismometer’ and vice versa, making it difficult to determine if differences in noise properties arise from the overall instrument package or sensor design in these cases. For example, T-240 sensors exist only in the B2 design, and CMG-3T sensors exist only in the BG and KE designs, which are simply distinguished by the presence or absence of an accelerometer, respectively. In addition, many of the individual sensors and other components have been in use for over a decade; small adjustments to instrument design and wear and tear may produce variability in data quality that is difficult to assess. A small number of colocated pilot deployments of BBOBS with different seismometers or instrument designs in shallow and deep locations could test the robustness of the results presented here. We also suggest that codeployments should be an essential aspect of testing new BBOBS designs whenever possible.

Our analysis is dependent on the accuracy of both data and metadata archived within the IRIS DMC, and one example of a colocated deployment suggests that errors may exist. The PLUME experiment (Doran & Laske 2019) utilized an intermixed array of T-240 and CMG-3T sensors in relatively deep water. The individual seismometer spectra (Figs S3 and S4) group into distinct clusters, with the T-240 s offset to significantly lower power at all bands. Given the similar deployment environment for these instruments, the simplest interpretation for the offset is a gain error. Based on the secondary microseism peak (0.1–1 Hz), the CMG-3Ts are biased ~ 10 dB too high, or the T-240 s are biased low. Doran & Laske (2019) analysed this apparent bias and calculated station-specific gain corrections of $\times 2$ or $\times 4$ for the PLUME T-240 observations.

Here, we take a more general approach to specifically assess whether such issues could significantly impact our analyses. We estimate that the T-240 data are biased approximately 10 dB low. This is based on the observations that the average T-240 spectrum is lower than our full-data set average in the secondary microseism band by approximately this amount (Fig. 6), and that several older T-240 experiments have low noise levels relative to more recent experiments using those same instruments, including in the secondary microseism band (Figs S3 and S4).

To test the impact of these gain uncertainties on our analysis, we collect all the T-240 spectra from these suspect experiments collected prior to 2011, and increase them by 10 dB. We then rerun the spectral-angle analysis, and compare the resulting groupings to

those presented above (Section 4.3). The dominant groupings are unchanged, as are the majority of the details of the spectral characteristics within each grouping. The weaker secondary microseism peak in the average T-240 spectrum is no longer present, but the T-240 spectrum at long periods remains lower than the other instruments, particularly for the Z and Z-corrected components. After this adjustment, the difference between the H component noise on the T-240 and T-Compact is minimal; however, both remain lower than the observed noise levels for the CMG-3Ts. This evaluation reassures us that our primary conclusions are robust in the face of metadata uncertainty of the scale suggested by Figs S3 and S4.

Finally, the limited duration of standard OBS deployments (≤ 12 months) means that our analysis is subject to the idiosyncrasies of experiment timing. As an example, the recording period for the HO-BITSS experiment on the Hikurangi forearc largely overlapped the 2014–2016 El Niño event, confounding our ability to assess the normative noise characteristics of this particular margin. In this study of overall trends, we have chosen not to consider seasonal variability of noise, which can be substantial (e.g. Stutzmann *et al.* 2009; Grob *et al.* 2011), and in addition we do not consider secular changes in noise with time (*cf.* Bell *et al.* 2015). Further, this study uses only instruments from U.S.-funded BBOBS deployments; many other designs exist that we have not included here. Their future inclusion would likely mitigate covariances between metadata parameters (particularly between seismometer and instrument design), and yield a wider geographic footprint.

As the marine geophysical community plans for long-term BBOBS observatories (Kohler *et al.* 2020), it would be worthwhile to invest resources in exploring the noise characteristics of these undersampled regions of metadata parameter space. The data set presented in this study assists in framing noise domain gaps that future pilot experiments could fill.

6 CONCLUSIONS

We have computed representative noise spectra for 551 broad-band BBOBS stations spanning 18 experiments deployed between 2005 and 2019, including seismic components and pressure gauges. We also calculated cross-spectral properties (admittance, phase, coherence) that help reveal and quantify seismic noise induced by bottom currents and infragravity waves. The resultant data set constitutes the most comprehensive sampling of noise characteristics at seafloor stations to date. Our analysis supplies a framework for BBOBS users to compare and assess the noise characteristics of individual data sets, better anticipate noise characteristics for newly acquired data, and provide a baseline catalogue that will continue to grow in detail and utility as the marine geophysics community expands BBOBS sampling of the world's diverse seafloor.

By grouping noise spectra based on metadata parameters, we demonstrate that there are significant systematics to BBOBS noise characteristics. The most important determinants of noise characteristics are the seismometer (which strongly covaries with instrument design), and the water depth at which it is deployed. Accounting for other factors, BBOBSs with CMG-3T seismometers seem to have higher low-frequency noise than average, and those with T-240 sensors have lower noise levels, particularly on the vertical components. CMG-3T instruments have higher tilt noise on the vertical components, most clearly seen at long periods, and overall, more noisy horizontals. Although noise is correlated with seismometer (and by extension instrument design) type, we find no systematic

orientation of the tilt noise, suggesting that none of the BBOBSs' engineering creates a bias in tilt direction.

We have shown, for the first time, that the theoretical depth-frequency limit for seafloor compliance is closely matched by the data spanning 0–6000 m in water depth. BBOBS deployed on continental shelves in shallow water (<500 m) have systematically different noise properties, characterized in particular by higher noise in the primary microseism band on all four components. The exception is shallow water lake instruments, which have low noise in the global microseism band, and a unique ~ 0.4 Hz peak. This and other departures from our main groupings will need to be re-evaluated in the future as new data sets provide wider sampling of station properties.

We found that grouping by experiment yielded the highest similarity of spectra, indicating that the combination of station parameters (similar instrumentation, geographic footprint, etc.) deterministically controls overall BBOBS noise. This holds promise for informed experiment planning; overall noise properties are station contingent, but largely predictable. Despite this, we recognize that our analysis is incomplete, limited by uneven global sampling, and covariance between important metadata parameters. Key future work may include systematic analysis of seasonal and other temporal variability, expansion of the data set to include additional instrument designs and deployment locations, including non-U.S.-funded deployments, buried or cabled instrumentation, and testing the effects of iterative noise removal procedures.

ACKNOWLEDGMENTS

Data used in this research were provided by instruments from the Ocean Bottom Seismic Instrument Center (<https://obsic.whoi.edu>) and the Ocean Bottom Seismograph Instrument Pool (OBSIP), funded by the National Science Foundation (<https://www.nsf.gov>). We thank the instrument centre staff at Woods Hole Oceanographic Institution (WHOI), Lamont Doherty Earth Observatory (LDEO) and Scripps Oceanographic Institution (SIO), as well as seagoing technicians and scientists who made collection of this data possible. These data are archived at the IRIS Data Management Center (<http://www.iris.edu>). This manuscript benefited from conversations with Spahr Webb, Kasey Aderhold, and James Lindsey. We also acknowledge the contributions of two anonymous reviewers whose thoughtful feedback improved this manuscript. This work was funded by National Science Foundation Awards OCE-1658491, OCE-1658214 and OCE-1753722.

AUTHOR CONTRIBUTION STATEMENT

HAJ designed and coordinated the study, carried out the processing and calculation of spectral properties for all instruments, organized all data for analysis. ZE assisted in study design and coordination of the writing. JR aided in processing of YOUNG ORCA data. BB, ZE, HAJ and SC designed and carried out the spectral angle analysis. HAJ, JR, ZE, JG, SM, WH each contributed to the collection of metadata parameters for the stations. All authors participated in interpretation and manuscript preparation.

DATA AVAILABILITY

The seismic and pressure time-series data are available for download through the IRIS Data Management Center (<http://www.iris.edu>).

The assembled station metadata table, and calculated spectral properties are available in the online supplementary material. Additionally, the calculated noise spectra and cross spectra, and metadata table is archived at Dryad (<https://doi.org/10.25349/D90042>). The ATaCR package used to process the data is available here: <https://github.com/helenjanisz/ATaCR>. Codes to complete the spectral angle analysis can be found here: <https://github.com/brennanbrunsvik/Ocean-bottom-seismometer-noise-clustering>. Codes to transfer data from ATaCR output to input for spectral analysis and other visualization can be found here: <https://github.com/helenjanisz/BBOBS-Noise>.

REFERENCES

- Accardo, N.J., *et al.*, 2017. Surface wave imaging of the weakly extended Malawi Rift from ambient-noise and teleseismic Rayleigh waves from onshore and lake-bottom seismometers, *Geophys. J. Int.*, **209**(3), 1892–1905.
- Aderhold, K., Woodward, R. & Frassetto, A., *Ocean Bottom Seismograph Instrument Pool, Final Report*, 2019. Zenodo.
- An, C., Wei, S.S., Cai, C. & Yue, H., 2020. Frequency limit for the pressure compliance correction of ocean-bottom seismic data, *Seismol. Res. Lett.*, **91**, 967–976.
- An, C., Cai, C., Zhou, L. & Yang, T., 2021. Characteristics of low-frequency horizontal noise of ocean-bottom seismic data, *Seismol. Res. Lett.*, **93**, 257–267.
- Ardhuin, F., Stutzmann, E., Schimmel, M. & Mangeney, A., 2011. Ocean wave sources of seismic noise, *J. geophys. Res.*, **116**(C9).
- Ardhuin, F., Rawat, A. & Aucan, J., 2014. A numerical model for free infragravity waves: definition and validation at regional and global scales, *Ocean Modelling*, **77**, 20–32.
- Ardhuin, F., Gualtieri, L. & Stutzmann, E., 2015. How ocean waves rock the Earth: two mechanisms explain microseisms with periods 3 to 300 s, *Geophys. Res. Lett.*, **42**, 765–772.
- Ardhuin, F., 2018. Large scale forces under surface gravity waves at a wavy bottom: a mechanism for the generation of primary microseisms, *Geophys. Res. Lett.*, **45**(16), 8173–8181.
- Aucan, J. & Ardhuin, F., 2013. Infragravity waves in the deep ocean: an upward revision, *Geophys. Res. Lett.*, **40**(13), 3435–3439.
- Babcock, J.M., Kirkendall, B.A. & Orcutt, J.A., 1994. Relationships between ocean bottom noise and the environment, *Bull. seism. Soc. Am.*, **84**, 1991–2007.
- Barchek, G., *et al.*, 2020. The Alaska amphibious community seismic experiment, *Seismol. Res. Lett.*, **91**(6), 3054–3063.
- Bécel, A., Laigle, M., Diaz, J., Montagner, J.-P. & Hirn, A., 2011. Earth's free oscillations recorded by free-fall OBS ocean-bottom seismometers at the Lesser Antilles subduction zone, *Geophys. Res. Lett.*, **38**(24), doi:10.1029/2011GL049533.
- Bell, S.W., Forsyth, D.W. & Ruan, Y., 2015. Removing noise from the vertical component records of ocean-bottom seismometers: results from year one of the Cascadia initiative, *Bull. seism. Soc. Am.*, **105**(1), 300–313.
- Bendat, J.S. & Piersol, A.G., 2010. *Random Data: Analysis and Measurement Procedures*, 4th edn, Wiley.
- Bird, P., 2003. An updated digital model of plate boundaries, *Geochim. Geophys. Geosyst.*, **4**(3).
- Bodmer, M., Toomey, D.R., Hooft, E.E., Nábělek, J. & Braunmiller, J., 2015. Seismic anisotropy beneath the Juan de Fuca plate system: evidence for heterogeneous mantle flow, *Geology*, **43**(12), 1095–1098.
- Bodmer, M., Toomey, D.R., Hooft, E.E. & Schmandt, B., 2018. Buoyant Asthenosphere Beneath Cascadia Influences Megathrust Segmentation, *Geophys. Res. Lett.*, **45**(14), 6954–6962.
- Boigatzis, P., Karamitrou, A., Neale, J.W., Harmon, N., Rychert, C.A. & Srokosz, M., 2020. Source Regions of infragravity waves recorded at the bottom of the equatorial Atlantic Ocean, using OBS of the PI-LAB experiment, *J. geophys. Res.*, **125**(6), doi:10.1029/2019JC015430.
- Bowden, D.C., Kohler, M.D., Tsai, V.C. & Weeraratne, D.S., 2016. Offshore Southern California lithospheric velocity structure from noise cross-correlation functions, *J. geophys. Res.*, **121**, 3415–3427.
- Bromirski, P.D., Duennbier, F.K. & Stephen, R.A., 2005. Mid-ocean microseisms, *Geochem., Geophys., Geosyst.*, **6**(4), doi:10.1029/2004GC000768.
- Cai, C., Wiens, D.A., Shen, W. & Eimer, M., 2018. Water input into the Mariana subduction zone estimated from ocean-bottom seismic data, *Nature*, **563**, 389–392.
- Carchedi, C.J.W., Gaherty, J.B., Webb, S.C. & Shillington, D.J., 2022. Investigating short-period lake-generated microseisms using a broadband array of onshore and lake-bottom seismometers, *Seismol. Res. Lett.*, **93**, 1585–1600.
- Collins, J.A. *et al.*, 2001. Broadband seismology in the oceans: lessons from the ocean seismic network pilot experiment, *Geophys. Res. Lett.*, **28**(1), 49–52.
- Collins, J.A., Wolfe, C.J. & Laske, G., 2012. Shear wave splitting at the Hawaiian hot spot from the PLUME land and ocean bottom seismometer deployments, *Geochem. Geophys. Geosyst.*, **13**(2), doi:10.1029/2011GC003881.
- Cox, C., Deaton, T. & Webb, S., 1984. A deep-sea differential pressure gauge, *J. Atmos. Ocean. Technol.*, **1**(3), 237–246.
- Crawford, W.C., Webb, S.C. & Hildebrand, J.A., 1991. Seafloor compliance observed by long period pressure and displacement measurements, *J. geophys. Res.*, **96**, 16 151–16 160.
- Crawford, W.C. & Webb, S.C., 2000. Identifying and removing tilt noise from low-frequency (<0.1 Hz) seafloor vertical seismic data, *Bull. seism. Soc. Am.*, **90**(4), 952–963.
- Crawford, W., Ballu, V., Bertin, X. & Karpytchev, M., 2015. The sources of deep ocean infragravity waves observed in the North Atlantic Ocean, *J. geophys. Res.*, **120**(7), 5120–5133.
- Deen, M., Wielandt, E., Stutzmann, E., Crawford, W., Barruol, G. & Sigloch, K., 2017. First observation of the Earth's permanent free oscillations on ocean bottom seismometers, *Geophys. Res. Lett.*, **44**, 10 988–10 996.
- Doran, A.K. & Laske, G., 2016. Infragravity waves and horizontal seafloor compliance, *J. geophys. Res.*, **121**(1), 260–278.
- Doran, A.K. & Laske, G., 2017. Ocean-bottom seismometer instrument orientations via automated Rayleigh-wave arrival-angle measurements, *Bull. seism. Soc. Am.*, **107**(2), 691–708.
- Doran, A.K., Rapa, M., Laske, G., Babcock, J. & McPeak, S., 2019. Calibration of differential pressure gauges through in situ testing, *Earth Space Sci.*, **6**, 2663–2670.
- Doran, A.K. & Laske, G., 2019. Seismic structure of marine sediments and upper oceanic crust surrounding Hawaii, *J. geophys. Res.*, **124**(2), 2038–2056.
- Eilon, Z., Abers, G.A., Jin, G. & Gaherty, J.B., 2014. Anisotropy beneath a highly extended continental rift, *Geochem. Geophys. Geosyst.*, **15**, 545–564.
- Eilon, Z.C. & Abers, G.A., 2017. High seismic attenuation at a mid-ocean ridge reveals the distribution of deep melt, *Sci. Adv.*, **3**(5), e1602829, doi:10.1126/sciadv.1602829.
- Essing, D., Schlindwein, V., Schmidt-Aursch, M.C., Hadzioannou, C. & Stähler, S.C., 2021. Characteristics of current-induced harmonic tremor signals in ocean-bottom seismometer records, *Seismol. Res. Lett.*, **92**, 3100–3112.
- Goncharov, A., Cooper, A., Chia, P. & O'Neil, P., 2016. A new dawn for Australian ocean-bottom seismography, *Leading Edge*, **35**(1), 99–104.
- Grob, M., Maggi, A. & Stutzmann, E., 2011. Observations of the seasonality of the Antarctic microseismic signal, and its association to sea ice variability, *Geophys. Res. Lett.*, **38**(11), doi:10.1029/2011GL047525.
- Hasselmann, K., 1963. A statistical analysis of the generation of microseisms, *Rev. Geophys.*, **1**(2), 177–210.
- Hawley, W.B., Allen, R.M. & Richards, M.A., 2016. Tomography reveals buoyant asthenosphere accumulating beneath the Juan de Fuca plate, *Science*, **353**(6306), 1406–1408.
- Hilmo, R. & Wilcock, W.S.D., 2020. Physical sources of high-frequency seismic noise on Cascadia initiative ocean bottom seismometers, *Geochem., Geophys., Geosyst.*, **21**(10), doi:10.1029/2020GC009085.

- International Hydrographic Organization, IHO, 1953. *Limits of Oceans and Seas*. International Hydrographic Organization, Special Publication No 23, 3rd edn, IMP, Monégasque - Monte-Carlo, pp. 45, doi:10013/epic.37175.d001.
- Janiszewski, H.A. & Abers, G.A., 2015. Imaging the plate interface in the Cascadia seismogenic zone: new constraints from offshore receiver functions. *Seismol. Res. Lett.*, **86**(5), 1261–1269.
- Janiszewski, H.A., Gaherty, J.B., Abers, G.A., Gao, H. & Eilon, Z.C., 2019. Amphibious surface-wave phase-velocity measurements of the Cascadia subduction zone, *Geophys. J. Int.*, **217**(3), 1929–1948.
- Jin, G., Gaherty, J.B., Abers, G.A., Kim, Y., Eilon, Z. & Buck, W.R., 2015. Crust and upper mantle structure associated with extension in the Woodlark Rift, Papua New Guinea from Rayleigh-wave tomography, *Geochem., Geophys., Geosyst.*, **16**(11), 3808–3824.
- Kohler, M.D. et al., 2020. A plan for a long-term, automated, broadband seismic monitoring network on the global seafloor, *Seismol. Res. Lett.*, **91**(3), 1343–1355.
- Laske, G., Markee, A., Orcutt, J.A., Wolfe, C.J., Collins, J.A., Solomon, S.C., Detrick, R.S., Bercovici, D. & Hauri, E.H., 2011. Asymmetric shallow mantle structure beneath the Hawaiian Swell—evidence from Rayleigh waves recorded by the PLUME network, *Geophys. J. Int.*, **187**(3), 1725–1742.
- Laurindo, L.C., Mariano, A.J. & Lumpkin, R., 2017. An improved near-surface velocity climatology for the global ocean from drifter observations, *Deep Sea Res. Part I: Oceanogr. Res. Papers*, **124**, 73–92.
- Leahy, G.M., Collins, J.A., Wolfe, C.J., Laske, G. & Solomon, S.C., 2010. Underplating of the Hawaiian Swell: evidence from teleseismic receiver functions, *Geophys. J. Int.*, **183**(1), 313–329.
- Lee, T.R., Wood, W.T. & Phrampus, B.J., 2018. Global derived datasets for use in k-NN machine learning prediction of global seafloor total organic carbon (Version 1) [Data set]. Zenodo. doi:
- Lin, P.Y., et al., 2016. High-resolution seismic constraints on flow dynamics in the oceanic asthenosphere, *Nature*, **535**, 538–541.
- Lior, I., et al., 2021. On the detection capabilities of underwater DAS, *J. geophys. Res.*, **126**(3), e2020JB020925, doi:10.1029/2020JB020925.
- Longuet-Higgins, M.S., 1950. A theory of the origin of microseisms, *Philos. Trans. R. Soc.*, **243**, 1–35.
- Lynner, C. & Bodmer, M., 2017. Mantle flow along the eastern North American margin inferred from shear wave splitting, *Geology*, **45**, 867–870.
- Mark, H.F., Collins, J.A., Lizarralde, D., Hirth, G., Gaherty, J.B., Evans, R.L. & Behn, M.D., 2021. Constraints on the depth, thickness, and strength of the G discontinuity in the central Pacific from S receiver functions, *J. geophys. Res.*, **126**, e2019JB019256, doi:10.1029/2019JB019256.
- Mazzullo, A., Stutzmann, E., Montagner, J.P., Kiselev, S., Maurya, S., Barruol, G. & Sigloch, K., 2017. Anisotropic tomography around La Réunion island from Rayleigh waves, *J. geophys. Res.*, **122**(11), 9132–9148.
- McNamara, D.E. & Buland, R.P.(2004). Ambient noise levels in the continental United States. *Bull. seism. Soc. Am.*, **94**(4), 1517–1527.
- Montagner, J.-P. et al., 1994. The French Pilot Experiment OFM-SISMOBS: first scientific results on noise level and event detection, *Phys. Earth planet. Inter.*, **84**(1–4), 321–336.
- Mosher, S.G., Eilon, Z.C., Janiszewski, H.A. & Audet, P., 2021. Probabilistic inversion of seafloor compliance for oceanic crustal shear velocity structure using mixture density neural networks, *Geophys. J. Int.*, **227**(3), 1879–1892.
- Müller, R.D., Sdrolias, M., Gaina, C. & Roest, R.W., 2008. Age, spreading rates, and spreading asymmetry of the world's ocean crust. *Geochem., Geophys., Geosyst.*, **9**(4), doi:10.1029/2007GC001743.
- Pawlowicz, R., 2020. "M.Map: a mapping package for MATLAB", version 1.4 m, [Computer software], available online at www.eoas.ubc.ca/~rich/map.html.
- Peterson, 1993. Observation and modeling of seismic background noise, U.S., Geol. Surv. Tech. Rept. 93-322, pp. 1–95.
- Purdy, G.M. & Orcutt, J.A., 1995. Broadband seismology in the oceans – towards a five-year plan, Ocean Seismic Net./Joint Oceanogr. Inst., Washington, D.C.
- Ruan, Y., Forsyth, D.W. & Bell, S.W., 2014. Marine sediment shear velocity structure from the ratio of displacement to pressure of Rayleigh waves at seafloor, *J. geophys. Res.*, **119**, 6357–6371.
- Russell, J.B., Gaherty, J.B., Lin, P.-Y.P., Lizarralde, D., Collins, J.A., Hirth, G. & Evans, R.L., 2019. High-resolution constraints on Pacific upper mantle petrofabric inferred from surface-wave anisotropy, *J. geophys. Res.*, **124**, 631–657.
- Rychert, C.A., Harmon, N. & Tharimena, S., 2018. Scattered wave imaging of the oceanic plate in Cascadia, *Sci. Adv.*, **4**(2), doi:10.1126/sciadv.aoa1908.
- Shinohara, M., Yamada, T., Shiobara, H. & Yamashita, Y., 2018. Development and evaluation of compact long-term broadband ocean bottom seismometer, in *2018 OCEANS-MTS/IEEE Kobe Techno-Oceans (OTO)*, pp. 1–4, IEEE.
- Smalls, P.T., Sohn, R.A. & Collins, J.A., 2019. Lake-bottom seismograph observations of microseisms in Yellowstone Lake, *Seismol. Res. Lett.*, **90**(3), 1200–1208.
- Sohn, Y. & Rebello, N.S., 2002. Supervised and unsupervised spectral angle classifiers, *Photogramm. Eng. Remote Sens.*, **68**(12), 1271–1280.
- Spica, Z.J., Nishida, K., Akuhara, T., Pétrélis, F., Shinohara, M. & Yamada, T., 2020. Marine sediment characterized by ocean-bottom fiber-optic seismology, *Geophys. Res. Lett.*, **47**(16), doi:10.1029/2020GL088360.
- Stephen, R.A. et al., 2003. Ocean seismic network pilot experiment, *Geochem., Geophys., Geosyst.*, **4**(10), doi:10.1029/2002GC000485.
- Stähler, S.C. et al., 2016. Performance report of the RHUM-RUM ocean bottom seismometer network around La Réunion, western Indian Ocean, *Adv Geosci.*, **41**, 43–63.
- Stähler, S.C., Aursch, M.C.S., Hein, G. & Mars, R., 2018. A self-noise model for the German DEPAS OBS pool, *Seismol. Res. Lett.*, **89**, 1838–1845.
- Straume, E.O. et al., 2019. GlobSed: updated total sediment thickness in the world's oceans, *Geochem., Geophys., Geosyst.*, **20**(4), 1756–1772.
- Stutzmann, E., Schimmel, M., Patau, G. & Maggi, A., 2009. Global climate imprint on seismic noise, *Geochem. Geophys. Geosyst.*, **10**(11), doi:10.1029/2009GC002619.
- Sumy, D.F., Lodewyk, J.A., Woodward, R.L. & Evers, B., 2015. Ocean-bottom seismograph performance during the Cascadia initiative, *Seismol. Res. Lett.*, **86**(5), 1238–1246.
- Tian, Y. & Ritzwoller, M.H., 2017. Improving ambient noise cross-correlations in the noisy ocean bottom environment of the Juan de Fuca plate, *Geophys. J. Int.*, **210**(3), 1787–1805.
- Tilmann, F.J. & Dahm, T., 2008. Constraints on crustal and mantle structure of the oceanic plate south of Iceland from ocean bottom recorded Rayleigh waves, *Tectonophysics*, **447**(1–4), 66–79.
- Toomey, D. et al., 2014. The Cascadia Initiative: a sea change in seismological studies of subduction zones, *Oceanography*, **27**(2), 138–150.
- Uchiyama, Y. & McWilliams, J.C., 2008. Infragravity waves in the deep ocean: generation, propagation, and seismic hum excitation, *J. geophys. Res.*, **113**(C7), doi:10.1029/2007JC004562.
- Wan, K.X., Vidavsky, I. & Gross, M.L., 2002. Comparing similar spectra: from similarity index to spectral contrast angle, *J. Am. Soc. Mass Spectrom.*, **13**(1), 85–88.
- Webb, S.C., Zhang, X. & Crawford, W., 1991. Infragravity waves in the deep ocean, *J. geophys. Res.*, **96**(C2), 2723–2736.
- Webb, S.C., Crawford, W.C. & Hildebrand, J.A., 1994. Long period seismometer deployed at OSN-1, seismic waves, **36**(1), 105–142.
- Webb, S.C., 1998. Broadband seismology and noise under the ocean. *Rev. Geophys.*, **36**(1), 105–142.
- Webb, S.C. & Crawford, W.C., 2010. Shallow-water broadband OBS seismology, *Bull. seism. Soc. Am.*, **100**(4), 1770–1778.
- Weeraratne, D.S., Forsyth, D.W., Yang, Y. & Webb, S.C., 2007. Rayleigh wave tomography beneath intraplate volcanic ridges in the South Pacific, *J. geophys. Res.*, **112**(B6), doi:10.1029/2006JB004403.
- Wei, S.S. et al., 2015. Seismic evidence of effects of water on melt transport in the Lau back-arc mantle, *Nature*, **518**(7539), 395–398.
- Wolfe, C.J. et al., 2009. Mantle shear-wave velocity structure beneath the Hawaiian Hot Spot, *Science*, **326**(5958), 1388–1390.

- Xu, Y., Koper, K.D. & Buracu, R., 2017. Lakes as a source of short period (0.5–2 s) microseisms, *J. geophys. Res.*, **122**, 8241–8256.
- Yang, Z., Sheehan, A.F., Collins, J.A. & Laske, G., 2012. The character of seafloor ambient noise recorded offshore New Zealand: results from the MOANA ocean bottom seismic experiment, *Geochem., Geophys., Geosyst.*, **13**(10), doi:10.1029/2012GC004201.
- Yang, X., Luo, Y., Xu, H. & Zhao, K., 2020. Shear wave velocity and radial anisotropy structures beneath the central Pacific from surface wave analysis of OBS records, *Earth planet. Sci. Lett.*, **534**, doi:10.1016/j.epsl.2020.116086.
- Zha, Y., Webb, S.C. & Menke, W., 2013. Determining the orientations of ocean bottom seismometers using ambient noise correlation, *Geophys. Res. Lett.*, **40**(14), 3585–3590.

SUPPORTING INFORMATION

Supplementary data are available at [GJI](#) online.

- Figure S1.** Deployment instrumentation and location histograms.
- Figure S2.** Deployment environmental properties histograms.
- Figure S3.** Vertical component noise spectra sorted by experiment.
- Figure S4.** Horizontal component noise spectra sorted by experiment.
- Figure S5.** Absolute pressure gauge component noise spectra sorted by experiment.
- Figure S6.** Differential pressure gauge component noise spectra sorted by experiment.
- Figure S7.** Corrected vertical component noise spectra sorted by experiment.
- Figure S8.** Horizontal-pressure coherences as a function of water depth.

Figure S9. Results of spectral angle grouping water-depth grid search.

Figure S10. Example of 3-layer spectral angle results for the vertical component.

Figure S11. Example of 3-layer spectral angle results for the horizontal component.

Figure S12. Example of 3-layer spectral angle results for the vertical corrected component.

Figure S13. Significance tests for spectral angle analysis.

Figure S14. Comparison of lake- and shelf-deployed shallow water vertical spectra.

Table S1. Information about the experiments that were used for our analysis. Includes appropriate citation information for data sets, as well as the network names under which the data is cataloged in the IRIS DMC.

Table S2. Assembled metadata parameter table for all examined instruments. A description of the source of the data, including references, is provided in the main text. This table also indicates if a particular channel was flagged as ‘good’ after quality control procedures, where a value of ‘1’ indicates the spectra was accepted and ‘0’ indicates it was discarded. Data Access: Calculated noise spectra and cross spectra, and metadata table is archived at Dryad, <https://doi.org/10.25349/D90042>.

Please note: Oxford University Press is not responsible for the content or functionality of any supporting materials supplied by the authors. Any queries (other than missing material) should be directed to the corresponding author for the paper.